

Research Paper

Design optimization and performance analysis of a dry-cooled Helium-Xenon Brayton cycle for nuclear microreactor based on detailed models of the cycle components

Chaoran Guan ^{a,b}, Xiang Chai ^{a,b,*}, Tengfei Zhang ^{a,b}, Hui He ^{a,b}, Xiaojing Liu ^{a,b}^a School of Mechanical Engineering, Shanghai Jiao Tong University, Shanghai 200240, China^b Shanghai Digital Nuclear Reactor Technology Integration Innovation Center, Shanghai, China

ARTICLE INFO

ABSTRACT

Keywords:

Dry-cooled closed Brayton cycle
 Nuclear microreactors
 He-Xe mixtures
 Cycle conceptual design
 Component preliminary design

Nuclear microreactors offer reliable, low-carbon dispatchable power and heat for various end use and applications. The gas-cooled reactor coupled with the dry-cooled closed Brayton cycle has a simple plant layout and can be deployed in water-deficient areas. To evaluate the system performance more precisely and optimize the mole fraction of the He-Xe mixture for the gas-cooled microreactor, an integrated design method based on detailed models of the cycle components was developed. Three designs using 4 g/mol pure helium, 15 g/mol, and 40 g/mol He-Xe were first established as demonstration examples, and performances of the cycle and components were compared. Furthermore, the effects of the He-Xe's molecular weight on the system's size and efficiency were discussed, and a parametric analysis of crucial design parameters like specific speed and pressure ratio was conducted. In contrast to the previous results obtained from simplified component models, the current results revealed that a Brayton cycle using 40 g/mol He-Xe could achieve a higher thermal efficiency of 44.42 % compared with 37.65 % of pure helium, which resulted from the improved efficiency in turbomachinery and reduced pressure loss in heat exchangers. Concerning the system size, it was recommended to use the 20–30 g/mol He-Xe for reduced volume as the stage number of the turbomachinery decreased from 5 of pure helium to a single stage of the 20 g/mol He-Xe. Although the turbomachinery occupied a relatively small volume, increasing the compressor inlet temperature could reduce the volume of the precooler, thus significantly reducing the system volume.

1. Introduction

Nuclear microreactors offer reliable, low-carbon dispatchable power and heat for various end-use applications [1]. They have disruptive potential as an alternative to carbon-intensive energy based on their mobility, transportability, resilience, and independence from the grid, as well as their capacity for long refueling intervals and low-carbon emissions [2]. As portable applications, microreactors can represent an option to restore power quickly in areas damaged by natural disasters or for humanitarian relief, for example, to support hospitals or local communities. Besides the low carbon dioxide emission, the main advantages of microreactors are considered to be small size, simple plant layout, and fast on-site installation [3]. They are being designed by several companies, and the gas-cooled reactor with a direct closed Brayton cycle is one of the design schemes, which can avoid the use of

the intermediate heat exchanger.

Helium (He) is the typical coolant of the high-temperature gas-cooled reactor (HTGR), which is being considered in the designs of Xenergy Xe-Mobile [4], BWXT BANR [5], HolosGen Holos Quad [6], Urenco U-Battery [7], Radian Kaleidos [8], USNC MMR [9], Nugen Engine [10]. Except for the latter two designs, the others all use a Brayton cycle as the energy conversion unit. As one of the Generation IV reactors, the HTGR has been intensively developed and is now in demonstration operation in China [11]. However, for large-scale HGTR, the steam Rankine cycle is used. A multi-stage turbomachinery is required for the helium Brayton cycle, which may conflict with the design objectives of small plant size for microreactors. To solve this problem, helium is mixed with a heavier noble gas to reduce the size and mass of the turbo-machines. This is because the number of stages of the compressor is inversely proportional to the molecular weight of the noble-gas mixture under the same design conditions [12]. Among the

* Corresponding author at: School of Mechanical Engineering, Shanghai Jiao Tong University, Shanghai 200240, China.

E-mail address: xiangchai@sjtu.edu.cn (X. Chai).

Nomenclature	
<i>Latin symbols</i>	
b	blade height [m]
B	aerodynamic blockage
C	capacitance rate [J/s/K]; absolute velocity [m/s]
C_θ	empirical blockage correction factor [-]
D	diameter [m]
e	peak-to-valley surface roughness
f	Fanning friction factor
G	mass flux [$\text{kg}/\text{s}\cdot\text{m}^2$]
h	specific enthalpy [J/kg]
HTC	heat transfer coefficient [$\text{W}/\text{k}\cdot\text{m}^2$]
H	height [m]
i	incidence angle [$^\circ$]
k_{eff}	multiplication factor of the reactor core
l	element length [m]
L	length [m]
m	mass flow rate [kg/s]
Ma	Mach number [-]
$minTTD$	minimum terminal temperature difference [K]
n	element number [-]
N	rotation speed [RPM]; number [-]
N_s	specific speed [-]
Nu	Nusselt number [-]
NTU	number of transfer units [-]
o	throat width [m]
p	balde pitch [m]
P	pressure [Pa]
Pr	Prandtl number [-]
Q	thermal power [W]
Re	Reynolds number [-]
S	heat transfer area [m^2]
t	blade thickness [m]
T	temperature [K]
t_e	effective conduction thickness [m]
u	fluid velocity [m/s]
UA	thermal conductance [W/K]
\dot{V}	volume flow rate [m^3/s]
W	width [m]; relative velocity [m/s]
Z	number of blades [-];
<i>Greek symbols</i>	
α	absolute flow angle with respect to the meridional direction [$^\circ$]
α_c	streamline slope angle with axis [$^\circ$]
β	relative flow angle with respect to the meridional direction [$^\circ$]
<i>Subscripts</i>	
a	axial
b	blade
cam	camberline
$comp$	compressor
ch	channel
hx	heat exchanger
m	meridional
ma	matrix
h	hydraulic
lmt	limit
pre	precooler
rcp	recuperator
rel	relative
RN	runner
opt	optimal
s	shroud; stall condition
t	tip
th	throat
<i>Superscripts</i>	
*	total condition; condition at minimum-loss incidence angle
<i>Abbreviations</i>	
DVS	downstream vaneless region
He-Xe	Helium-Xenon mixture
HTGR	High-Temperature Gas-cooled Reactor
LE	leading edge
PCHE	Printed Circuit Heat Exchanger
$s\text{CO}_2$	supercritical carbon dioxide
TAC	Turbine-Alternator-Compressor
UVS	upstream vaneless region
TE	trailing edge
Tol	tolerance

noble-gas binary mixtures, He-Xe is commonly chosen due to its excellent heat transfer performance, especially for space nuclear reactors, where space is highly confined [1314].

Besides small system sizes, the feasibility of dry cooling in the Brayton cycle is also worth considering. It is very likely for micro-reactors to be deployed at places where water resources are scarce, given the potential applications including military installations, off-grid markets, and locations recovering from natural disasters. In this regard, the Radian Kaleidos design aims to achieve zero on-site water use by leveraging fans for air cooling [8]. Kim et al. [15] designed a micro modular reactor, in which indirect air cooling is adopted. Moisseytsev et al. [16] developed a crossflow compact Printed Circuit Heat Exchanger (PCHE) for the dry-cooled $s\text{CO}_2$ Brayton cycle because the compact counterflow heat exchanger required a large air circulation

power.

There have been some studies on the analysis and optimization of the Brayton power cycle for nuclear reactors. Sondelski & Nelis [17] conducted a mass optimization for a $s\text{CO}_2$ Brayton cycle with a direct cooled nuclear reactor, in which masses of the recuperator and radiator were calculated based on empirical correlations. It was found that the radiator mass dominates the total mass, and a working fluid with a higher critical temperature might be more suitable given that typical advantages of the $s\text{CO}_2$ systems were not realized. Similarly, Miao et al. [18] performed an optimization of the Brayton cycle for the space nuclear system. The mass of the turbo-alternator was calculated based on an empirical expression, and the results showed that the proposed $\text{N}_2\text{O}-\text{He}$ mixture had superior performance compared with N_2O and CO_2 alone. Luo & Huang [19] investigated the thermodynamic and exergoeconomic performances of

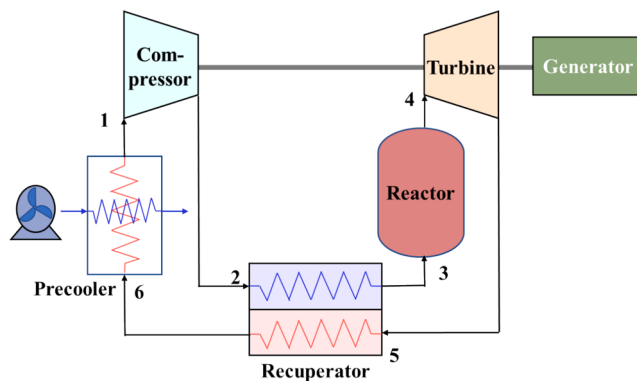


Fig. 1. The layout of the simple regenerative cycle.

various Brayton cycles for next-generation nuclear reactors, in which the PCHE was modeled based on the one-dimensional model while other components used the zero-dimensional model. It was concluded that the recompression cycle performed the most outstanding in terms of total product unit cost among the studied cycles. Rao et al. [20] performed a multi-objective optimization of the sCO₂ recompression cycle. A one-dimensional method was used in the preliminary design of PCHE in their studies, and the cycle was optimized in terms of thermal efficiency and total cost. Liu et al. [21] optimized a He-Xe Brayton cycle for the space nuclear reactor system, in which the heat exchanger was modeled by the one-dimensional method, while the mass of the reactor was set constant. Du et al. [22] optimized the efficiency, cost, and volume of a sCO₂ recompression cycle for the small lead-cooled fast reactor. In their study, Baljie's diagram was used to estimate the efficiency and diameter of the turbo-machines, and a one-dimensional method was employed for the preliminary design of the heat exchanger. Consequently, the trade-off result between the three objectives was obtained.

As mentioned above, simplified models of either heat exchangers or turbo-machines have been adopted in most of them. The coupling effect between the cycle and component design requires more realistic models to precisely evaluate the system's performance. In this regard, Saeed et al. [23] utilized mean-line codes for the turbomachinery along with a one-dimensional method for the heat exchanger to investigate the performance of a sCO₂ recompression cycle. Results revealed that the conventional cycle simulation method based on non-isentropic single equation models of the turbomachinery overpredicted or underpredicted the cycle's performance. Likewise, Yao & Zou [24] proposed a one-dimensional methodology based on the integration of the cycle design and component preliminary design for the sCO₂ recompression cycle. Cycles at different power levels were designed and their performances were analyzed and compared. Son et al. [25] investigated the feasibility of a solar-hybrid system for distributed power sources considering both cycle and component designs. The mean-line method was used to estimate the off-design performances of the hybrid system. Furthermore, this system was re-designed by optimizing solar to nuclear ratio while tracing changes in the levelized cost [26].

Based on the preceding discussion, it can be concluded that more detailed models of the turbomachinery and heat exchanger are required for precisely evaluating the performance of the Brayton cycle. To the best of our knowledge, such a methodology concerning the dry-cooled Brayton cycle has not been presented in the literature, and the performance of the He-Xe gas-cooled microreactor system has not been evaluated based on detailed component models, though it was deduced to have smaller turbomachinery and heat exchanger but with reduced thermal efficiency. To fill this gap, an integrated design method of the dry-cooled Brayton cycle for nuclear microreactors has been developed and implemented based on detailed component models. The mean-line design code was used to obtain the geometry and performance of the turbomachinery at various design conditions. The one-dimensional

discretization was employed for the preliminary design of the PCHE and thermal-hydraulic calculation of the gas-cooled reactor, while the two-dimensional method was used for sizing the precooler.

The structure of this paper is as follows: Section 2 outlines the layout and flow chart for the modeling of the Brayton cycle. Also, detailed descriptions of the reactor core, recuperator, precooler, and turbomachinery models are presented. Section 3 presents the validation results of the Brayton cycle modeling and preliminary design methods for the heat exchanger and turbomachinery. Section 4 first demonstrates detailed design results of pure helium, 15 and 40 g/mol He-Xe. Based on this, the performances of different He-Xe mixtures in terms of thermal efficiency and system volume are further compared. In addition, the impacts of key design parameters on system performance are analyzed. Finally, conclusions are drawn in Section 5.

2. System modeling and assumptions

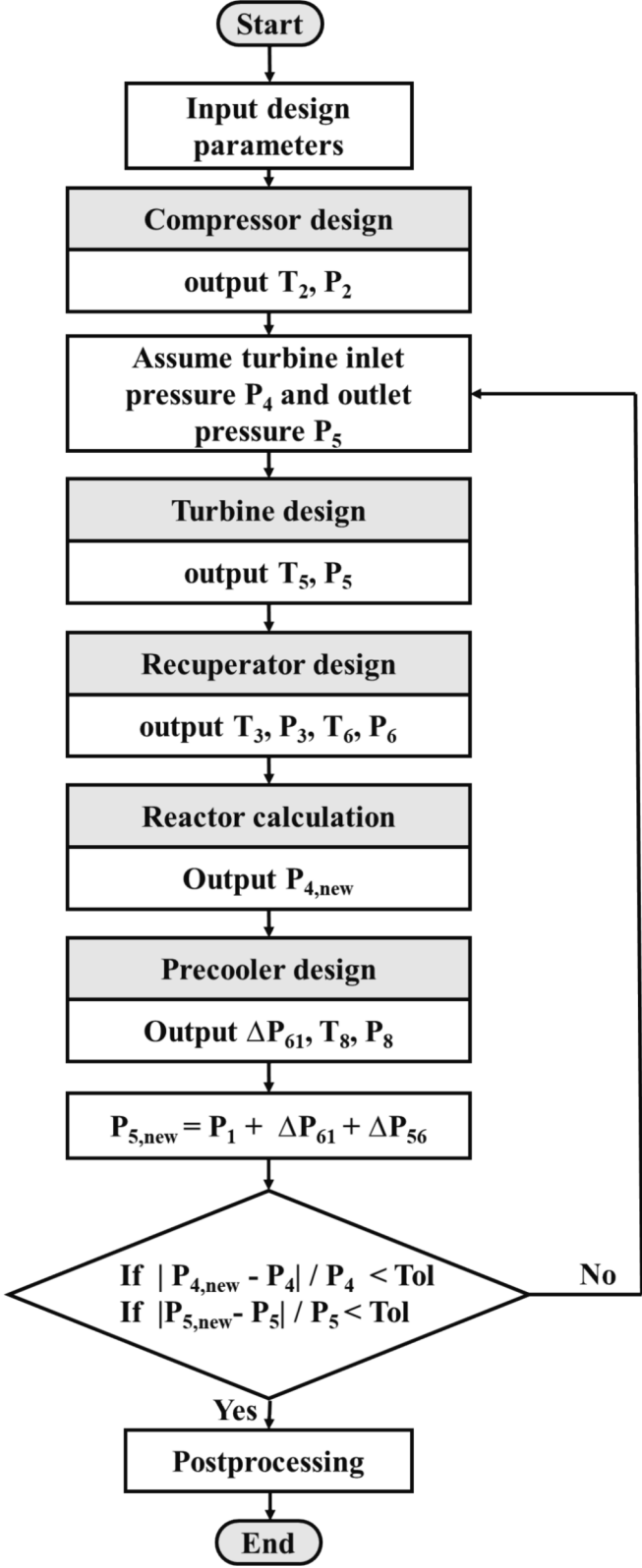
2.1. System description and assumption

The present study employed a simple regenerative cycle, which has a simple plant layout to meet the design requirements of small size and fast on-site installation. It consists of the gas-cooled nuclear reactor, recuperator, precooler, and turbomachinery as depicted in Fig. 1. The reactor is directly connected to a dry-cooled Brayton cycle, and hence the use of an intermediate heat exchanger is avoided. The gas-cooled reactor employed the prismatic block, which is made of graphite and serves as the moderator to slow down the neutrons. Turbomachinery for Brayton cycles can be configured in many ways, and in theory, the simplest solution is to package all elements within the same high-pressure casing [27]. Considering the requirement of the simple plant layout and existing designs from the literature, a Turbine-Alternator-Compressor (TAC) configuration was selected, which represents that the turbine, compressor, and generator are coaxial. Therefore, the same rotation speed was set during the design of the compressor and turbine. The PCHE was adopted as the recuperator. They are constructed from flat metal plates, into which fluid flow channels are photo-chemically etched into one side of the plate. Extensive research has settled on the choice of using PCHE as a recuperator of the Brayton cycle, due to its compactness, reliable mechanical characteristics at high pressure and temperature, and high effectiveness [28]. However, for the dry-cooled Brayton cycle, using PCHE as a precooler would require a large power for air circulation. As one of the solutions, a conceptual crossflow PCHE was proposed, which effectively reduced the pressure drop on the air side while still maintaining a compact structure [28]. Its structure will be described in detail in Section 2.4.

The calculation of He-Xe's thermodynamic and transport properties used the method developed by Tournier & El-Genk [29]. Additionally, The modeling process adopted the following assumptions:

- The gravitational effects are ignored.
- The heat loss and pressure drop in the pipelines and junctions are neglected.
- Pressure drop due to the entrance and exit loss is neglected, and only frictional loss and acceleration effect along the channel are considered.
- The kinetic energy in the heat exchanger and reactor is neglected.

The calculation models of each component were integrated into the thermodynamic calculation of the simple regenerative cycle, as shown in Fig. 2. Since the expansion ratio of the turbine depends on the pressure losses of the reactor core and heat exchanger, an iterative procedure was adopted. The preliminary design of the compressor is conducted prior to the iteration loop given that the inlet temperature and pressure of the compressor remain unchanged based on user inputs. Then, the inlet pressure and outlet pressures of the turbine are assumed, and the turbine design is performed, which outputs the outlet temperature and

**Fig. 2.** Flow chart for the simple recuperation design.

pressure. Consequently, the inlet conditions of the recuperator are obtained, and the outlet conditions are calculated through its preliminary design. Next, the reactor model takes the outlet temperature and pressure from the recuperator's cold side as inlet conditions. Also, the outlet temperature of the reactor core is taken as input referring to typical

Table 1
Geometric specification of the nuclear reactor.

Parameter	Value	
Basic unit	Fuel material	Uranium carbide
	Enrichment	19.75 %
	Moderator material	Graphite
	Fuel pin diameter [cm]	1.4
	Coolant channel diameter [cm]	0.8
	High-pressure tube thickness [cm]	0.1
	Fuel-to-coolant pitch [cm]	1.5
Reactor core	Reactor core diameter [m]	0.78
	Reactor core height [m]	1.0
	Reflector material	Beryllium
	Axial reflector thickness [m]	0.2
	Radial reflector thickness [m]	0.3
	k_{eff}	1.10227
	(Standard deviation)	(±0.00032)
	Cycle length [EFPYs]	10

outlet temperatures of HTGRs. Together with the specified geometric parameters, the reactor model calculates its thermal power and pressure loss. Then, the precooler model takes the outlet temperature from the recuperator's hot side and calculates the required dimensions to cool the He-Xe flow to a target temperature before the compressor inlet. Finally, the turbine inlet pressure and expansion ratio can be updated based on the newly calculated pressure losses of components. The above calculation is repeated until the inlet and outlet pressures of the turbine converge.

2.2. Gas-cooled nuclear reactor

The gas-cooled nuclear reactor used the design from our previous work [30] as summarized in Table 1. The effective multiplication factor k_{eff} calculated using the Monte Carlo software OpenMC [31] was 1.10227, which allows operation for about 10 years without refueling at a power level of 20 MWe. The layout of the reactor core is illustrated in Fig. 3. Channels are drilled through the graphite matrix to accommodate the high-pressure tubes and fuel rods. The fission heat released by the fuel rods is transferred to the gas coolant inside the high-pressure tube. The reactor core is surrounded by axial and radial reflectors to reduce neutron leakage. The dimension of the reactor core remained unchanged, which guaranteed the sufficient k_{eff} value. In addition, the maximal temperature of the high-pressure tube was noticed during the thermal-hydraulic calculation to make sure it was below 1400 K [32].

The thermal-hydraulic calculation of the reactor core employed a one-dimensional discretization approach as illustrated in Fig. 3. This method assumes a uniform mass flow rate and power distribution in the radial direction. The input parameters of the reactor model included the inlet temperature ($T_{core,in}$), inlet pressure ($P_{core,in}$), outlet temperature ($T_{core,out}$), and geometric specifications, which were used to determine the distributions of the temperature and pressure, as well as thermal power (Q). A cosine distribution was assumed for the axial power distribution, and hence the outlet temperature of the coolant for element i was calculated by

$$Q = \dot{m}(h_{out,core} - h_{in,core}) \quad (1)$$

$$h_{i+1} = h_i + \frac{\int_{z_i}^{z_{i+1}} \frac{Q}{H} \times \frac{\pi}{2} \cos(\frac{\pi z}{H}) dz}{\dot{m}_{ch}} \quad (2)$$

where h_i is specific enthalpy, z_i is the axial coordinate of the element, \dot{m} is the mass flow rate.

According to the convective heat transfer process, the surface temperature of the tube was calculated by

$$T_{tube,i+1} = T_{core,i+1} + \frac{q_l \cdot \pi / 2 \cos(\pi z_{i+1} / H)}{A \cdot HTC_{i+1}} \quad (3)$$

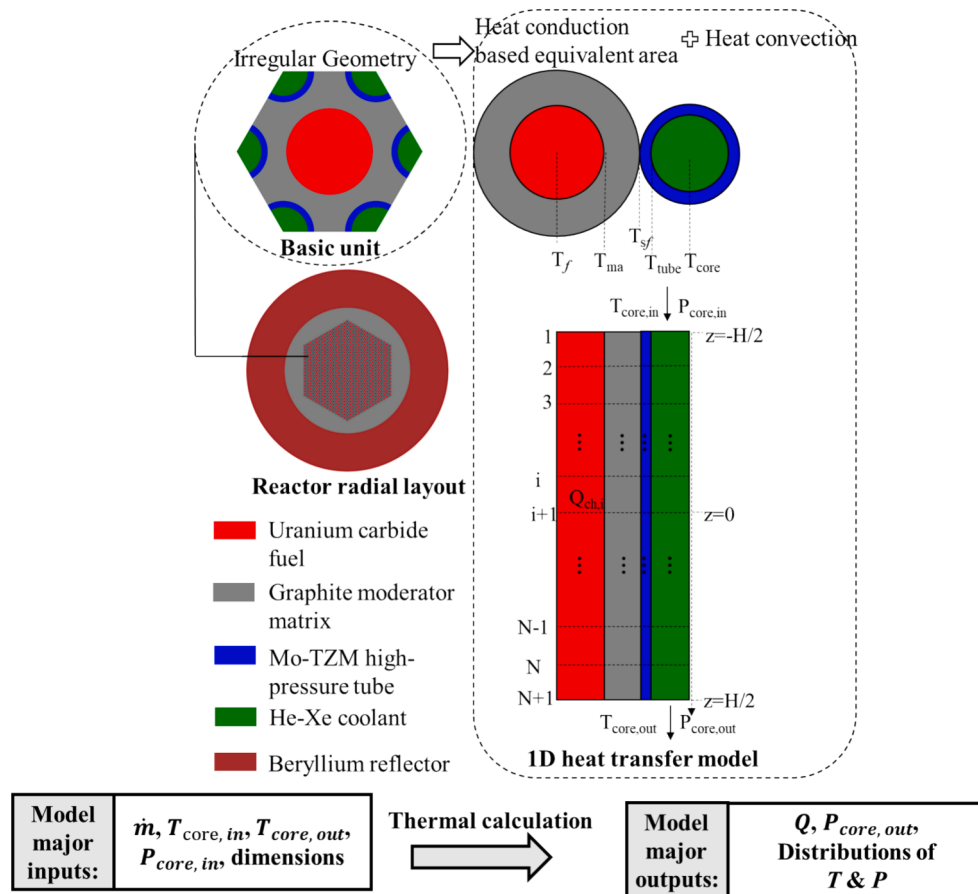


Fig. 3. Schematic diagram of the one-dimensional reactor model.

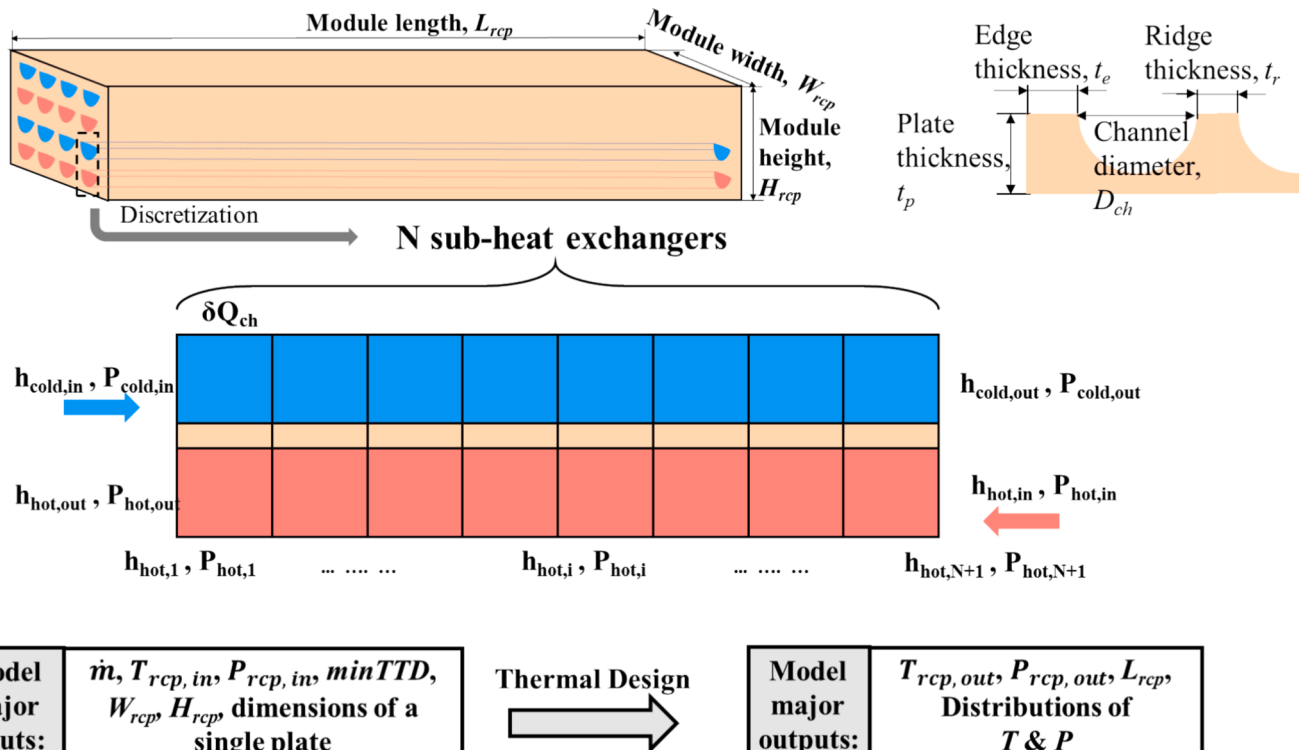


Fig. 4. Schematic diagram of the recuperator model.

Table 2

Geometric specifications of a single PCHE plate for recuperator.

Parameter	Value
Material	IN740H
Channel diameter [mm]	2
Channel pitch [mm]	2.4
Ridge thickness [mm]	0.4
Plate thickness [mm]	1.684
Edge thickness [mm]	0.61

where, $T_{core,i+1}$ is the coolant temperature, A is the heat transfer area per unit length. HTC_{i+1} is the heat transfer coefficient, which was calculated using the Nusselt number

$$Nu_i = \frac{HTC_i D_{ch}}{\lambda_{heXe,i}} \quad (4)$$

where D_{ch} is the inner diameter of the coolant channel, $\lambda_{heXe,i}$ is the thermal conductivity of the He-Xe mixture. The empirical correlations for the He-Xe's Nusselt number referred to the work of Dragunov et al [33], which are summarized in Appendix A.

The pressure drop of the He-Xe flow was calculated by

$$P_{i+1} = P_i - \frac{f_i}{2} \frac{\delta l_i}{D_{in}} \rho_i u_i^2 - G^2 \left(\frac{1}{\rho_{i+1}} - \frac{1}{\rho_i} \right) \quad (5)$$

where the first term on the right-hand side of the equation represents the frictional loss, and the second term is the accelerational loss. δl_i is the element length, ρ_i is the fluid density, u_i is the velocity, G is the mass flux, f is the friction factor using the Colebrook-white correlations, which are summarized in Appendix A.

2.3. PCHE

A one-dimensional discretization model was employed for the preliminary design of the recuperator as demonstrated in Fig. 4. The input parameters included the inlet temperature ($T_{rcp,cold,in}$, $T_{rcp,hot,in}$), inlet

pressure ($P_{rcp,cold,in}$, $P_{rcp,hot,in}$), minimum terminal temperature difference ($minTTD$), module width (W_{rcp}), module height (H_{rcp}), and geometric specifications of a single plate. Using these inputs, the required module length (L_{rcp}) was calculated as well as the distributions of the temperature and pressure. The geometric specifications of a single plate are summarized in Table 2. The recuperator design used the high-temperature nickel-based alloy IN740H, and with the channel diameter specified as 2 mm, the thicknesses at different locations were obtained through mechanical design. Detailed calculation of the stress for the mechanical design referred to the work of Lian et al. [34].

In the recuperator model, the heat transfers of all channels were assumed to be identical. The heat transfer rate per channel was equally allocated to each sub-heat exchanger, and hence the outlet temperature of element i was calculated by [20]

$$h_{c,i+1} = h_{c,i} + \frac{Q_{rcp}}{N_{ch} \cdot n \cdot \dot{m}} \quad (6)$$

where $h_{c,i}$ is the specific enthalpy on the cold side. $Q_{rcp} = \dot{m}(h_{c,out} - h_{c,in})$ is the total heat duty of the recuperator, and the outlet enthalpy $h_{c,out}$ was obtained using the $minTTD$, $h_{c,out} = H(T_{h,in} - minTTD, p_{c,out})$. N_{ch} is the number of cold channels, n is the number of the sub-heat exchangers.

Next, the thermal conductance was calculated using the effectiveness-NTU method by [20]

$$UA_i = NTU \cdot C_{min} \quad (7)$$

$$NTU = \begin{cases} \frac{\log(\frac{1-\epsilon C_R}{1-\epsilon})}{1-C_R}, & \text{if } C_R \neq 1 \\ \frac{\epsilon}{1-\epsilon}, & \text{otherwise} \end{cases} \quad (8)$$

$$C_R = \frac{C_{min}}{C_{max}} \quad (9)$$

where NTU is the dimensionless number of transfer units for each sub-heat exchanger, ϵ is the effectiveness, C is the capacitance rate.

Finally, the length of each sub-heat exchanger was determined by

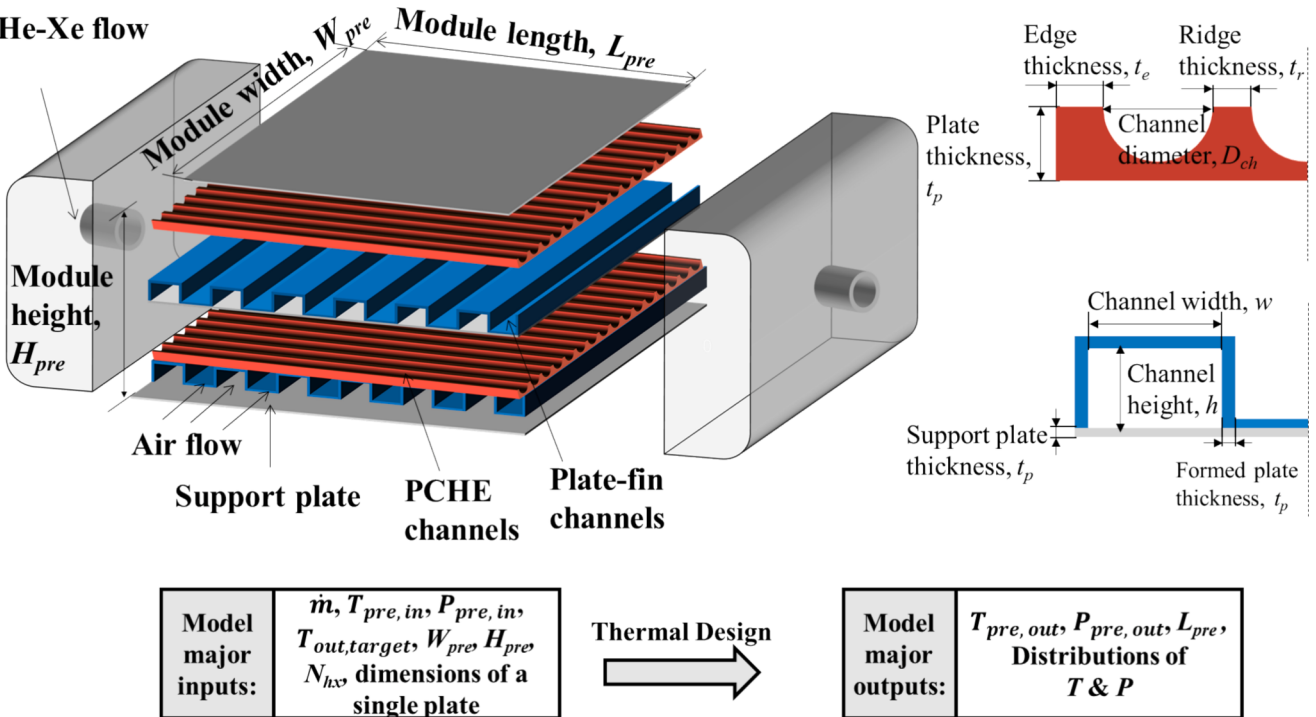
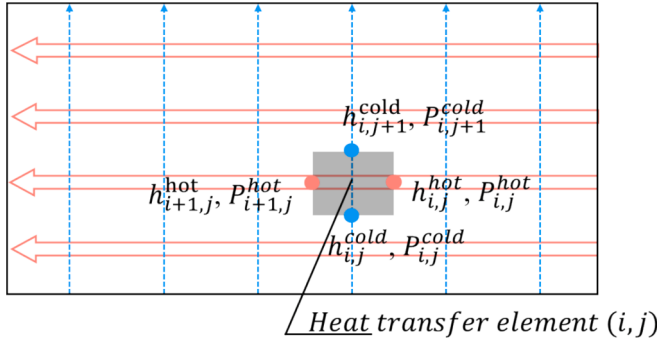


Fig. 5. Crossflow hybrid PCHE for the precooler.

Table 3

Geometric specifications of the plate for precooler.

Parameter	Value
Material PCHE side	IN740H
	Channel diameter [mm]
	2.0
	Channel pitch [mm]
	2.2
	Ridge thickness [mm]
Plate-fin side	0.2
	Plate thickness [mm]
	1.3
	Edge thickness [mm]
	0.3
	Channel height [mm]
Plate-fin side	4.0
	Channel width [mm]
	6.0
	Support plate thickness [mm]
Form plate thickness [mm]	0.3
	0.3

**Fig. 6.** Two-dimensional temperature fields of the precooler model.

$$\delta l_i = \frac{UA_i}{U_i \cdot (\pi D_{ch}/2 + D_{ch})} \quad (10)$$

where U_i is the overall heat transfer coefficient determined based on the convective heat transfer and heat conduction,

$$\frac{1}{U_i} = \frac{1}{HTC_{hot,i}} + \frac{t_e}{\kappa} + \frac{1}{HTC_{cold,i}} \quad (11)$$

where κ is the thermal conductivity of the plate, $t_e \approx 0.575D_{ch}$ is the equivalent thickness. The HTC is the heat transfer coefficient calculated using Eq. (4). Likewise, Eq. (5) was used to calculate the pressure drop for the PCHE channels. Empirical correlations for the calculation of the He-Xe Nusselt number and friction factor in the PCHE model were the same as those used in the gas-cooled reactor model.

2.4. Crossflow PCHE

The precooler utilized a crossflow hybrid PCHE, as shown in Fig. 5. It is a conceptual design, which combines traditional PCHE with plate-fin heat exchangers [16]. The He-Xe flows through the microchannels of the PCHE, while the cooling air flows through rectangular channels of plate fins. Besides the large flow area, the air flows widthwise to further reduce its pressure drop and required fan power. The major inputs of the precooler model included the inlet temperatures ($T_{air,in}, T_{pre,in}$), inlet pressures ($P_{air,in}, P_{pre,in}$), the target outlet temperature on the hot side, module width (W_{pre}), module height (H_{pre}), number of heat exchangers in parallel (N_{hx}), and geometric specifications of a single plate. According to the inputs, the required module length (L_{pre}) was calculated to cool the He-Xe flow to a target temperature before the compressor inlet. The geometric specifications of a single plate are presented in Table 3. The height and width of the rectangular channel were specified as 4.0 mm and 6.0 mm, and thicknesses at crucial locations were obtained through mechanical calculation to make sure they could withstand the stress under the working pressure. The method for stress calculation referred to the work of Lian et al. [34].

The heat transfer of each plate was assumed to be identical, and

hence the preliminary design of the precooler was conducted based on a pair of cold and hot plates. Additionally, the channel-outlet pressures were averaged to obtain a common outlet pressure. This assumption was partially justified by the fact that differences in pressure drops of these channels are not large [16]. A two-dimensional temperature field was used as illustrated in Fig. 6, where the red lines represent the semi-circular channels of the PCHE plate, and blue lines represent the air channels. The node number on the hot side was specified by the user input, whereas that on the air side was determined by the number of semicircular channels.

An iterative procedure was employed to search the required module length for the precooler as shown in Fig. 7. First, the initial length of the precooler was estimated. Subsequently, the outlet conditions were calculated based on the two-dimensional model. If the outlet temperature on the hot side failed to match the target one, the precooler length would be adjusted. The calculation was repeated until the outlet temperature converged to the target one. The calculation of the two-dimensional field began with the element at the entrance of the bottom channel (i.e. the bottom-right element in Fig. 6). After completing the calculation of element (i, j) , the calculation progressed to element $(i + 1, j)$ until reaching the outlet of channel j and then proceeded to the next channel $i + 1$. The empirical correlations adopted here for the He-Xe mixture.

were the same as those in the reactor and PCHE model, while for the air flow the correlations referred to the work of Moisseytsev & Sienicki [35], which are summarized in Appendix A.

2.5. Turbomachinery

Configuration (axial or radial) of the turbomachinery mainly depends on the flow rate, available enthalpy head, and cycle power level [2336]. The radial-type turbomachinery was considered for the nuclear microreactor system in this study. Fig. 8(a) illustrates the meridional view of the single-stage centrifugal compressor and radial turbine. The single stage consists of the rotor, stator (i.e. vaned diffuser for the compressor and nozzle for the turbine), and volute. Multistage is connected by the return channel, which consists of the crossover, vaned region, and exit bend. The limitation of the maximum impeller tip speed was taken as 500 m/s during the preliminary design of the turbomachinery [37].

A mean-line design code was used for the preliminary design of the turbomachinery. The one-dimensional mean-line method utilizes the calculation of fluid conditions before and after each component along an average streamline, which is assumed to be located in the mid-height of the blades for simplicity. Consequently, any variation in either fluid properties or the blade performance along the blade height is not considered.

The flow chart of the turbomachinery preliminary design is shown in Fig. 9. The input parameters for the turbomachinery model included the specific speed (N_s), mass flow rate (\dot{m}), inlet conditions (T^*, P^*), and pressure ratio (π). The rotation speed of the turbomachinery was obtained by the definition of the specific speed,

$$N_s = \frac{\mathbf{N}\sqrt{\dot{V}}}{(\Delta h_{is}^*)^{0.75}} \quad (12)$$

where Δh_{is}^* is the isentropic enthalpy drop, and \dot{V} is the volume flow rate (runner outlet for the turbine, and runner inlet for the compressor).

As shown in Fig. 9, the preliminary design of the turbomachinery consists of two steps: component sizing and performance analysis. The component sizing method referred to the work of Yao & Zou [24] as summarized in Appendix B. To achieve the required pressure ratio, adjustment was made to the isentropic loading coefficient ψ_{is} . As the runner sizing process was based on machine efficiency η , iteration of η was also included. To calculate the efficiency of the turbomachinery,

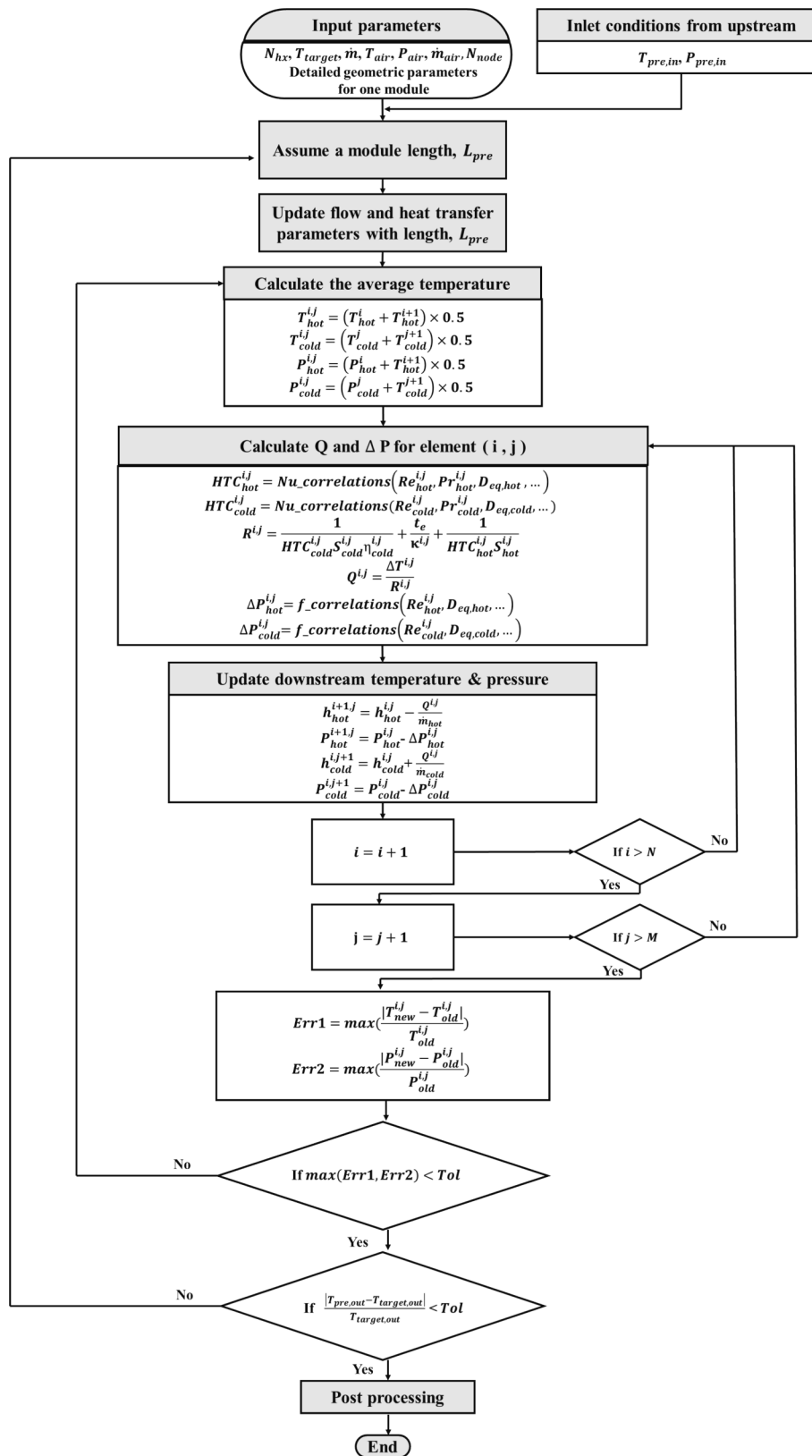


Fig. 7. Flow chart of the precooler design model.

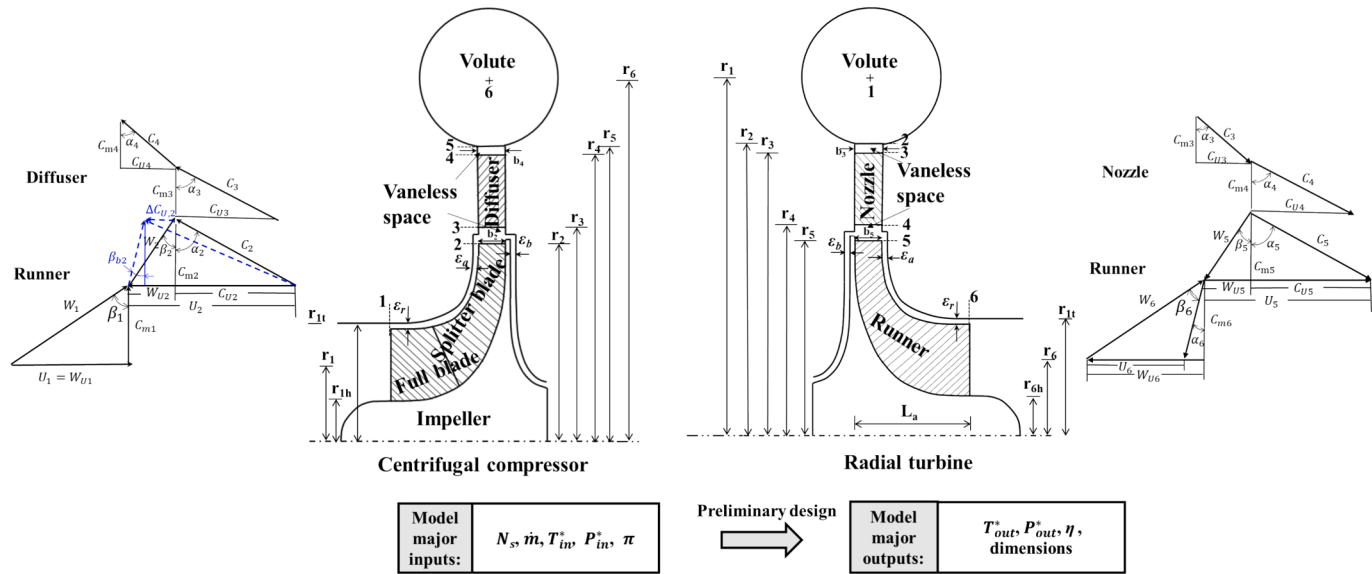


Fig. 8. Meridional view of the turbomachinery.

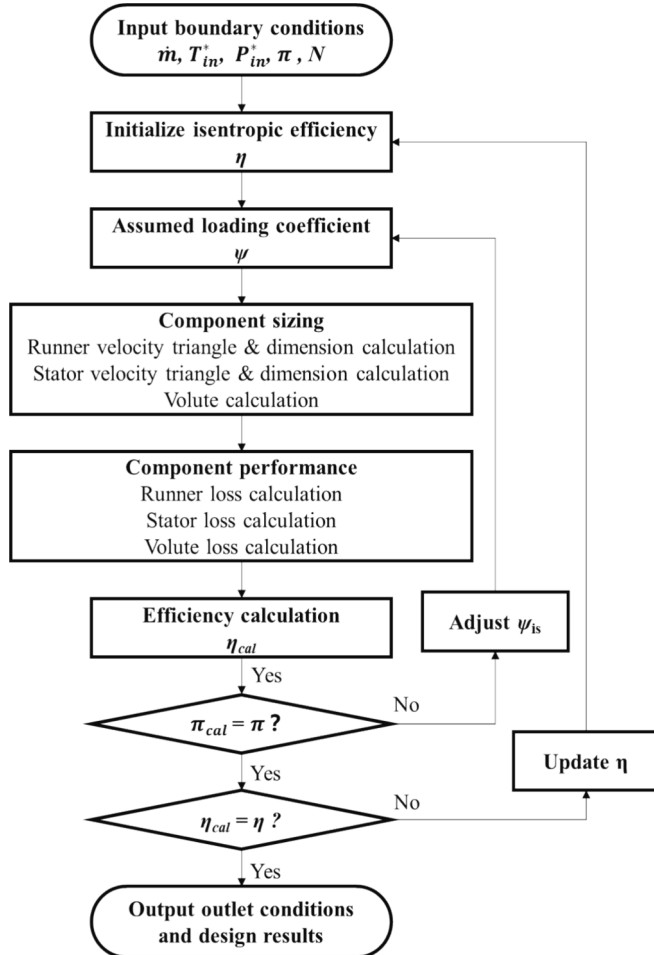


Fig. 9. Flow chart of the turbomachinery design.

Table 4
Validation results of the thermodynamic model for the Brayton cycle.

Input parameters	He [12]	40 g/mol He-Xe [12]
Compressor inlet temperature [K]	301.15	301.15
Compressor outlet pressure [MPa]	7	7
Compressor pressure ratio [-]	2.10	2.36
Compressor efficiency [-]	0.903	0.901
Turbine inlet temperature [K]	1173.15	1173.15
Turbine efficiency [-]	0.924	0.923
Recuperator efficiency [-]	0.95	0.93
Results		
Cycle efficiency of Literature [%]	45.84	43.60
Cycle efficiency of this work [%]	45.82	43.57
Error [%]	0.04	0.07

Table 5
Validation results of the heat exchanger model.

Input parameters		Value	
PCHE	T _{in} [K]	682.89 (hot side)/338.24 (cold side)	
	P _{in} [MPa]	9.33 (hot side)/17.92 (cold side)	
Results			
T _{out,hot} [K]	Literature [28]	This work	Deviation
T _{out,cold} [K]	350.94	350.95	0.003 %
ΔP _{hot} [kPa]	657.19	659.42	0.3 %
ΔP _{cold} [kPa]	52.00	51.01	1.9 %
	17.52	17.64	0.7 %
Crossflow hybrid PCHE	T _{in} [K]	362.75 (hot side)/303.15 (air side)	
	P _{in} [MPa]	7.64 (hot side)/0.102 (air side)	
Results			
T _{out,hot} [K]	Literature [16]	This work	Deviation
T _{out,cold} [K]	305.85	306.02	0.06 %
ΔP _{hot} [kPa]	308.39	307.76	0.2 %
ΔP _{cold} [Pa]	0.267	0.263	1.5 %
	139	136	2.2 %

Table 6
Validation results of the mean-line design code for the turbomachinery.

Inputs	Value		
Centrifugal compressor	T_{in}^* [K]	305.4	
	P_{in}^* [MPa]	7.69	
	Pressure ratio [-]	1.8	
	m [kg/s]	3.67	
	N [RPM]	75,000	
	Results	Literature [39]	This work
Radial inflow turbine	Outer diameter [mm]	37.3	36.75
	Design efficiency [%]	66.5	67.84
	T_{in}^* [K]	811.15	
	P_{in}^* [MPa]	13.58	
	Expansion ratio [-]	1.63	
	m [kg/s]	2.47	
Results	N [RPM]	75,000	
	Outer diameter [mm]	68.3	67.52
	Design efficiency [%]	85	85.16
	Literature [39]		This work
	Deviation		1.5 %
	Deviation		2.0 %

Table 7
Design inputs of the He-Xe gas-cooled microreactor system.

Parameter	Value
Molecular weight of working fluid \bar{M} [g/mol] [12]	4.0 (pure helium), 15, 40
Minimum cycle temperature T_{min} [K]	308.15
Maximum cycle temperature T_{max} [K] [37]	1123.15
Maximum cycle pressure P_{max} [MPa] [1237]	7
Compressor pressure ratio π [-] [1237]	2.1
Compressor specific speed N_s [-]	0.7
Recuperator $minTTD$ [K] [12]	22
Ambient air temperature [K]	303.15

loss models summarized in Appendix B, were utilized, which referred to the work of Yao & Zou [24] and Aungier RH [38]. For the stator and the volute, the actual process can be regarded as the composition of firstly an isentropic process and then an isobaric process. Thus, outlet conditions were calculated using Eq. (13) and Eq. (14).

$$h_{out,is}^* = h_m^* - \Delta h_{loss,ST}^* \quad (13)$$

$$P_{out}^* = P_{out,is}^* = P(h_{out,is}^*, s_{in}^*) \quad (14)$$

For the runner, due to the existence of the external loss $h_{RN,ex}^*$, the actual process is the composition of an ideal process and an isobaric process as shown in Eq. (15) and Eq. (16).

$$h_{out,is}^* = h_m^* \pm \Delta h_{Euler}^* - \Delta h_{loss,int}^* \quad (15)$$

Table 8
Comparison of the cycle performances.

Parameters	4 g/mol (pure helium)	15 g/mol	40 g/mol
Cycle power [MW _e]	8.0	8.0	8.0
Thermal power [MW _t]	21.26	20.13	18.00
Thermal efficiency	37.65 %	39.75 %	44.42 %
System volume [m ³]	22.92	18.44	18.95
Power density [MW _e /m ³]	0.349	0.434	0.422

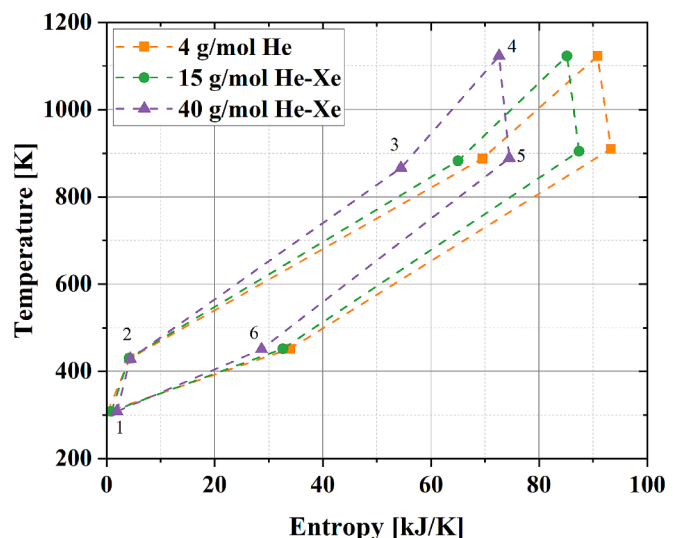
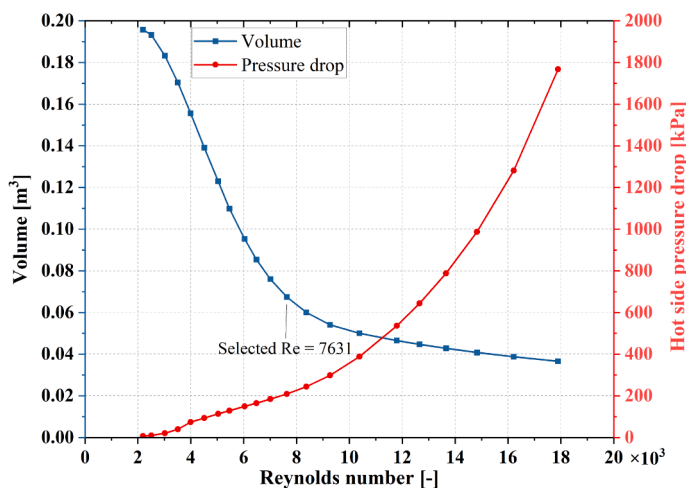
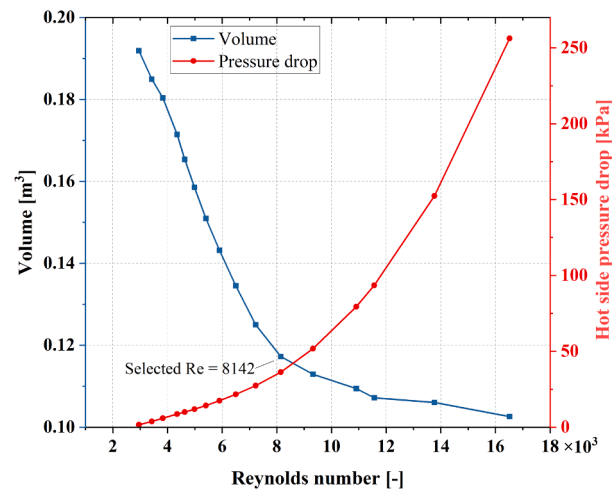


Fig. 11. The T-S diagram of three working fluids.



(a) Recuperator



(b) Precooler

Fig. 10. The selection of the inlet Reynolds number for heat exchangers.

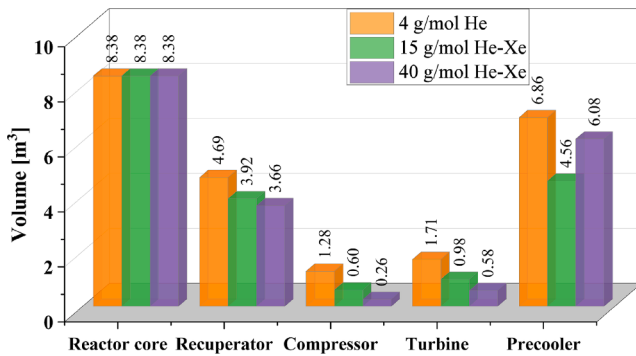


Fig. 12. Volumes of different components.

Table 9
Design results of the recuperators.

Parameters	Values		
Molecular weight [g/mol]	4	15	40
minTTD [K]	22	22	22
Heat duty [MW]	40.80	37.78	30.70
Module Width [m]	0.90	0.90	0.90
Module Height [m]	0.93	1.48	2.04
Module Length [m]	5.63	2.94	2.00
Hot/Cold inlet temperature [K]	908.93/433.34	904.60/431.08	888.49/428.79
Hot/Cold outlet temperature [K]	455.75/886.93	453.07/882.60	450.79/866.49
Hot/Cold side pressure drop [kPa]	283.00/153.46	329.21/168.13	211.92/106.79
Hot/Cold side inlet Reynolds number	3.03×10^3 / 5.07×10^3	5.24×10^3 / 8.91×10^3	7.63×10^3 / 13.07×10^3

$$h_{out}^* = h_{out,is}^* + \Delta h_{loss,int}^* + \Delta h_{loss,ext}^* \quad (16)$$

Therefore, the turbomachinery efficiency was calculated by

$$\eta = \frac{h_{in}^* - h_{out,is}^*}{h_{in}^* - h_{out}^*} \quad (\text{compressor}) \quad \text{or} \quad \frac{h_{in}^* - h_{out}^*}{h_{in}^* - h_{out,is}^*} \quad (\text{turbine}) \quad (17)$$

3. Model validation

The current work involved thermodynamic calculation of the Brayton cycle and preliminary design of the heat exchanger as well as the turbomachinery. Thus, the validations were performed for them both. When verifying the thermodynamic model of the Brayton cycle, the cycle maximum temperature, pressure, efficiency, and pressure drop of components from the reference were used as input, and the thermal efficiency was calculated and compared. Table 4 shows the validation

Table 10
Design results of the precoolers.

Parameters	Value		
Molecular weight [g/mol]	4	15	40
Target T _{hot,out} [K]	308.15	308.15	308.15
Heat duty [MW]	13.26	12.13	10.00
Module number in parallel [-]	72	76	54
Module width [m]	0.2	0.2	0.2
Module height [m]	0.11	0.18	0.4
Module length [m]	4.32	1.67	1.42
Air mass flow rate [kg/s]	402.84	423.57	299.51
Fan power [kWe]	224.47	466.55	121.31
Hot/Cold inlet temperature [K]	455.75/ 303.15	453.08/ 303.15	450.79/ 303.15
Hot/Cold outlet temperature [K]	308.15/ 335.89	308.15/ 331.56	308.15/ 336.32
Hot/Cold side pressure drop [kPa]	147.59/ 0.490	55.99/0.969	34.82/0.356
Hot/Cold side inlet Reynolds number [-]	4.05×10^3 / 4.58×10^3	6.41×10^3 / 7.06×10^3	8.26×10^3 / 3.75×10^3

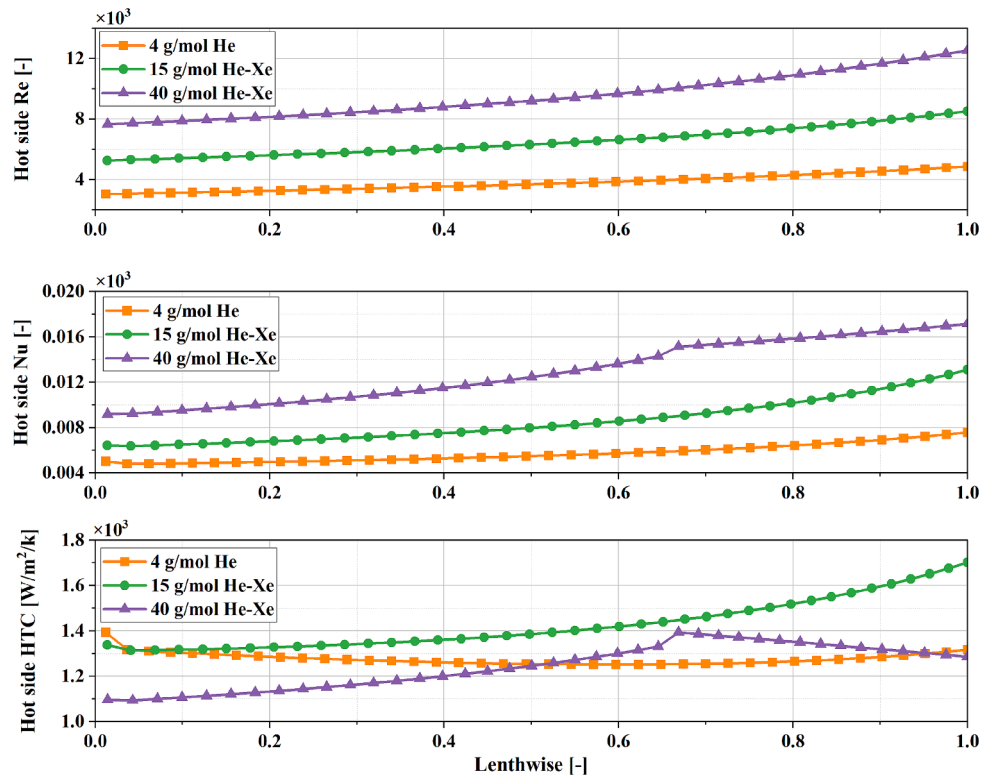


Fig. 13. Lengthwise distributions of Nu, Re, and HTC of the recuperators.

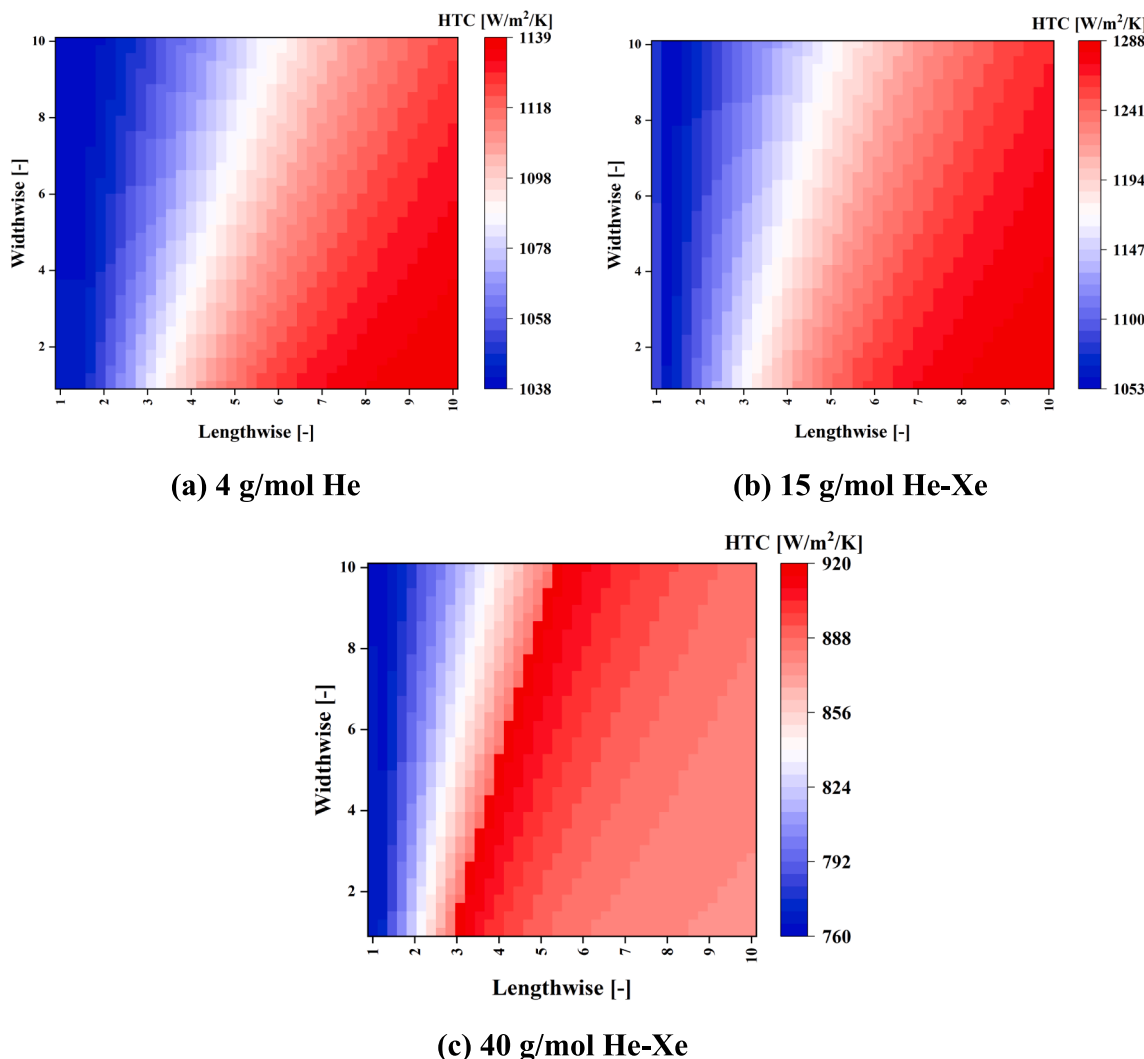


Fig. 14. HTC distributions of the precoolers.

results of the thermodynamic model, in which the maximum error of thermal efficiency is only 0.07 %.

For verifying the heat exchanger models, geometric specifications and inlet conditions were used as inputs and the calculated outlet conditions were compared with the reference. Table 5 shows the validation results of the heat exchanger model, in which the maximum error is 2.2 % from the pressure loss calculation of the precooler's air side. This could be caused by the differences in the fluid libraries and number of the calculation nodes.

For validating the mean-line design code of the turbomachinery, input parameters included the inlet conditions, mass flow rate, rotation speed, and target pressure ratio. The calculated efficiency and radius were compared with the reference. As displayed in Table 6, the maximum error is 2.0 % from the compressor's efficiency. These dissimilarities could result from the differences in the fluid property libraries and loss models of the turbomachinery. In summary, the developed model is deemed accurate enough to simulate the performance of the Brayton cycle.

4. Results and discussion

4.1. Design points and specification

In order to demonstrate the detailed design results, the pure helium (4 g/mol) and two He-Xe mixtures including 15 g/mol and 40 g/mol

were considered. Among them, 15 g/mol He-Xe is considered to have a better heat transfer coefficient, and 40 g/mol He-Xe has an equivalent heat transfer coefficient to pure helium [12]. The major design inputs of the cycle are summarized in Table 7. Most of the design options were referenced from the design option from literature. The temperature of the ambient air was assumed to be 303.15 K, and the lowest temperature of the cycle (compressor inlet) was set to 5 K higher than the ambient temperature. The outlet pressure of the compressor was set at 7 MPa with a pressure ratio of 2.1 [1237]. The turbine inlet temperature was chosen as 1123.15 K, corresponding to the typical outlet temperature of an HTGR [37].

Besides the above design inputs, the module width and height of the recuperator as well as the precooler were also required for the detailed model of the heat exchanger. Therefore, pre-calculations to balance the volume and pressure drop at different cross sections (i.e. inlet Reynolds numbers) were performed. Fig. 10 plots variations of heat exchanger volume and pressure drop under different inlet Reynolds numbers, in which the molecular weight of He-Xe is 40 g/mol. The cross sections of the precooler and recuperator were changed by varying the module height while fixing the width. As the inlet Reynolds number becomes larger, the HTC as well as the flow velocity is increased. This leads to smaller volumes and higher pressure losses of the heat exchanger. For example, when the inlet Reynolds number of the recuperator is 17.9×10^3 , the corresponding heat exchanger volume is 0.037 m^3 , but the pressure drop reaches 1767.2 kPa. Excessive pressure loss in the loop

Table 11
Design results of the compressors.

Parameters	Values		
Molecular weight [g/mol]	4	15	40
Type	Centrifugal	Centrifugal	Centrifugal
Stage number [-]	5	2	1
Rotation speed [RPM]	20,091	16,171	15,646
Mass flow rate [kg/s]	17.34	60.39	134.29
Total-to-total pressure ratio [-]	2.1	2.1	2.1
Total-to-total isentropic efficiency [-]	83.83 %	85.91 %	87.06 %
Work [MW]	11.275	10.285	8.464
Diameter [m]	1.07	1.11	1.04
Length [m]	1.398	0.605	0.287
Maximum impeller tip speed [m/s]	485.37	385.58	338.06
Flow coefficient [-]	0.0306	0.0433	0.0629
Rotor	Full blade (last stage for multistage)	10	10
Splitter blade number [-]	10	10	10
Inlet radius [m]	0.074	0.080	0.081
LE blade height [m]	0.041	0.048	0.053
LE blade angle [°]	-49.62°	-49.51°	-50.11°
LE blade thickness [mm]	3.07	3.20	3.33
Outlet radius [m]	0.231	0.228	0.206
Outlet blade height [m]	0.016	0.022	0.022
TE blade angle [°]	-49.99°	-49.98°	-50.01°
TE blade thickness [mm]	2.76	3.04	3.01
Axial Length [m]	0.079	0.080	0.094
Stator	Blade number [-]	10	10
(last stage for multistage)	Blade height [m]	0.016	0.022
Blade length [m]	0.294	0.300	0.241
Inlet radius [m]	0.231	0.228	0.231
LE blade angle [°]	71.68°	73.54°	69.95°
LE blade thickness [mm]	5.73	5.86	4.73
Outlet radius [m]	0.384	0.379	0.327
TE blade angle [°]	65.11°	64.66°	63.28°
TE blade thickness [mm]	5.73	5.86	4.73
Volute	Inlet radius [m]	0.384	0.379
Inlet blade height [m]	0.016	0.022	0.022
Full-collection plane radius [m]	0.461	0.468	0.433
Volute meridian radius [m]	0.077	0.089	0.090

will reduce the turbine expansion ratio, resulting in a smaller cycle efficiency. Taking both aspects into consideration, the inlet Reynolds number for the recuperator using 40 g/mol He-Xe was set at 7.63×10^3 . For the precooler, the fan power was calculated as $W_{fan} = \dot{m}_{air} \Delta P_{air} / (\rho_{air} \eta_{fan})$, in which the fan efficiency η_{fan} was taken as 75 %. When varying the height of the precooler, the air mass flow rate was kept constant. As a result, a small module height not only increased the pressure loss within the cycle but also increased the pressure drop of the air flow as well as the fan power. The inlet Reynolds number of the precooler was set at around 8.14×10^3 , of which the pressure loss on the air side was 338.1 Pa.

Table 8 displays the cycle performances of three working fluids, and their T-S diagrams are shown in Fig. 11. All three designs have an output power of 8 MWe, and the 40 g/mol He-Xe achieves the highest thermal efficiency of 44.42 %, while pure helium has the lowest, 37.65 %. As shown in the T-S diagram, the cycle of the 40 g/mol He-Xe has the lowest entropy loss, which is mainly influenced by the isentropic efficiencies of the turbo-machines and pressure losses in heat exchangers. From the perspective of power density, the highest value is 0.434 MWe/m³ of the 15 g/mol He-Xe. The corresponding total volume is 18.44 m³, which refers to the volume sum of the major components. The power density of the 40 g/mol He-Xe is slightly lower, 0.422 MWe/m³, where the increase

Table 12
Design results of the turbines.

Parameters	Values		
Molecular weight [g/mol]	4	15	40
Type	Radial	Radial	Radial
Stage number [-]	5	2	1
Rotation speed [RPM]	5	2	15,646
Mass flow rate [kg/s]	20,091	16,171	134.29
Total-to-total expansion ratio [-]	1.817	1.824	1.893
Total-to-total isentropic efficiency [-]	90.44 %	91.57 %	92.67 %
Work [MW]	19.277	18.285	16.463
Diameter [m]	1.094	1.211	1.855
Length [m]	1.807	0.844	0.462
Maximum impeller tip speed [m/s]	471.78	391.95	354.72
Flow coefficient [-]	0.3006	0.3108	0.3377
Rotor	Full blade number [-] (stage 1 for multistage)	14	13
Inlet radius [m]	0.220	0.229	0.216
LE blade height [m]	0.037	0.042	0.043
LE blade angle [°]	0.00°	0.00°	0.00°
LE blade thickness [mm]	2.20	2.29	2.16
Outlet radius [m]	0.084	0.096	0.106
Outlet blade height [m]	0.087	0.094	0.092
TE blade angle [°]	-56.23°	-57.75°	-60.32°
TE blade thickness [mm]	2.20	2.29	2.16
Stator	Axial Length [m]	0.147	0.151
(stage 1 for multistage)	Blade number [-]	25	23
Blade height [m]	0.037	0.042	0.043
Inlet radius [m]	0.274	0.293	0.290
LE blade angle [°]	58.32°	56.63°	53.78°
LE blade thickness [mm]	2.47	2.81	3.15
Volute	Outlet radius [m]	0.237	0.250
Outlet blade height [m]	0.037	0.042	0.043
Full-collection plane radius [m]	0.415	0.455	0.464
Volute meridian radius [m]	0.133	0.153	0.165

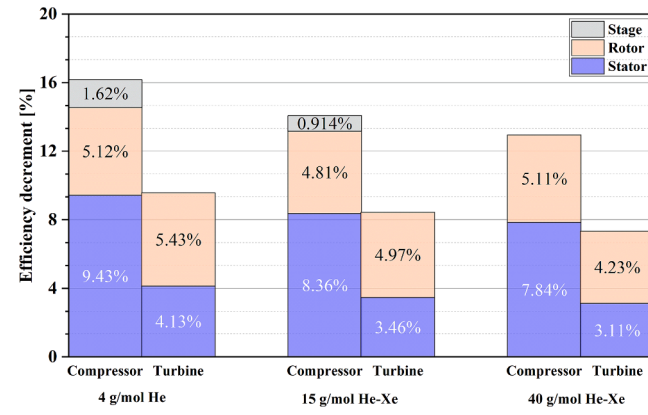


Fig. 15. Efficiency decrement of the turbomachinery.

in volume compared to that of the 15 g/mol He-Xe comes from the precooler. Fig. 12 shows the volumes of different components. As the molecular weight of He-Xe increases, the volumes of the recuperator and turbo-machines both decrease. However, the volume of the precooler for 15 g/mol is significantly lower than those of the other two. This is mainly because of the choice of inlet Reynolds number of the precooler, which will be discussed later in the design results of the precooler.

The design results for the recuperator are presented in Table 9. The

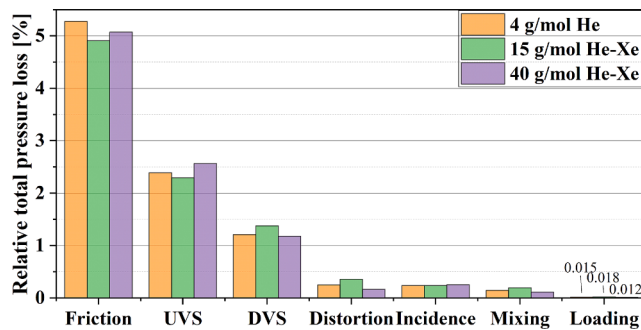


Fig. 16. Loss distributions of the compressor stator.

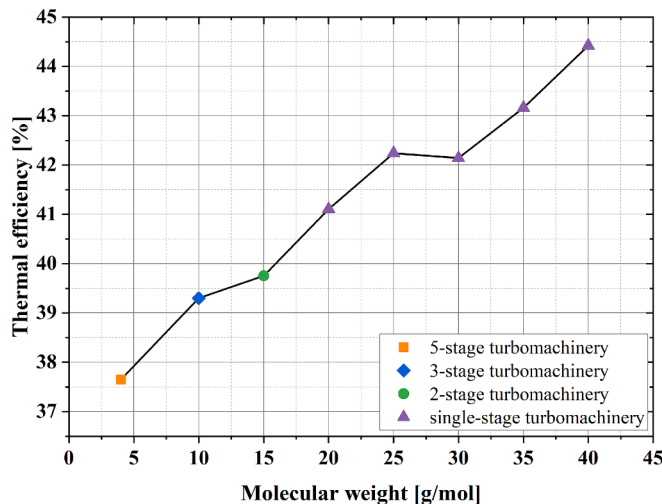


Fig. 17. Thermal efficiency of different He-Xe mixtures.

Table 13
Performances of different components.

Molecular weight [g/mol]	Turbomachinery efficiency		Relative pressure loss		
	Compressor	Turbine	Recuperator	Reactor	Precooler
4	83.83 %	90.44 %	6.235 %	0.0083 %	2.108 %
10	84.77 %	91.27 %	6.420 %	0.0158 %	1.330 %
15	85.92 %	91.57 %	7.105 %	0.0219 %	0.800 %
20	87.52 %	92.69 %	6.783 %	0.0262 %	1.153 %
25	86.89 %	92.69 %	6.094 %	0.0286 %	0.641 %
30	86.98 %	92.70 %	6.312 %	0.0338 %	0.558 %
35	87.03 %	92.66 %	5.493 %	0.0359 %	0.560 %
40	87.06 %	92.67 %	4.553 %	0.0364 %	0.497 %

minTTDs of all three recuperators are set at 22 K. The width and height of the heat exchanger are determined by the selection of the inlet Reynolds number as mentioned earlier. The one-dimensional model calculated the heat duty and required length of the recuperator based on the inlet conditions. As the molecular weight increases, the improved thermal efficiency results in a reduction of the heat input to the cycle. Consequently, the heat regeneration and the volume of the recuperator gradually decrease. Concerning the power density of the recuperator, the highest value is 9.64 MWt/m³ of 15 g/mol He-Xe, while those of pure helium and 40 g/mol He-Xe are 8.70 MWt/m³ and 8.39 MWt/m³, respectively. Apart from the temperature difference between the hot and cold sides, the power density of the recuperator is mainly influenced by the convective HTC. Fig. 13 illustrates the lengthwise distributions of Reynolds number, Nusselt number, and HTC of the recuperators. It can be observed that the HTC of 15 g/mol is higher than those of the other

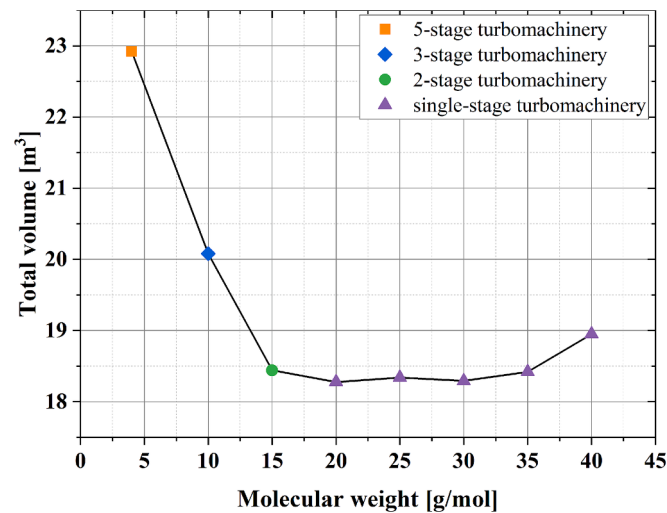


Fig. 18. The total volume of different He-Xe mixtures.

Table 14
Volumes of different components.

He-Xe mixture [g/mol]	Volume [m³]				
	Compressor	Recuperator	Reactor	Turbine	Precooler
4	1.2807	4.6909	8.3760	1.7100	6.8634
10	0.9287	4.6292	8.3760	1.3488	4.7966
15	0.6032	3.9178	8.3760	0.9844	4.5604
20	0.1998	3.5086	8.3760	0.4415	5.7509
25	0.2046	3.3259	8.3760	0.4621	5.9714
30	0.2366	3.1573	8.3760	0.5555	5.9672
35	0.2509	3.3506	8.3760	0.5652	5.8770
40	0.2569	3.6605	8.3760	0.5781	6.0834

two, and the HTC of 40 g/mol He-Xe surpasses that of pure helium at a normalized length of around 0.5. Moreover, the HTC of 40 g/mol starts to decrease at a normalized length of 0.7. This is because when the Reynolds number exceeds 1×10^4 , the growth rate of the Nusselt number slows down, and the decrease in the thermal conductivity makes the HTC begin to drop.

Table 10 provides the design results of the coolers. Multiple modules were connected in parallel to serve as the cooler to cool the hot fluid to 308.15 K using the ambient air. The module numbers were adjusted based on the heat duty so that a similar outlet temperature of the air flow was achieved. The module width was fixed at 0.2 m, while the height was determined by balancing the volume and pressure drop at different inlet Reynolds numbers, as mentioned earlier. The required module length was hence searched for the target $T_{hot,out}$, and the heat duty of the cooler was calculated. It should be noted that the outlet temperatures in Table 10 represent the average temperature. This is because the heat exchanger is arranged in a crossflow configuration, resulting in non-uniform temperature distribution at the outlet. For instance, in the cooler of 40 g/mol He-Xe, the outlet temperature range on the hot side is 304.11–313.75 K, while that on the cold side is 307.55–400.79 K. Although the heat duty of the cooler decreases as the molecular weight of He-Xe increases, the minimum volume of the cooler is 4.56 m³ of 15 g/mol He-Xe. Meanwhile, the power density of the 15 g/mol cooler is the highest at 2.65 MWt/m³, while those of pure helium and 40 g/mol He-Xe are 1.94 MWt/m³ and 1.64 MWt/m³, respectively. This is mainly influenced by HTCs on both the hot and cold sides of the cooler. Fig. 14 compares the HTC distributions on the hot side of the coolers. The HTC range of 15 g/mol He-Xe is 1053–1288 W/m²/K, slightly higher than that of pure helium. In addition, the HTCs on the air side for the cooler of 15 g/mol He-Xe are also larger, which are 181–195 W/m²/K due to the smaller flow area. In contrast, for

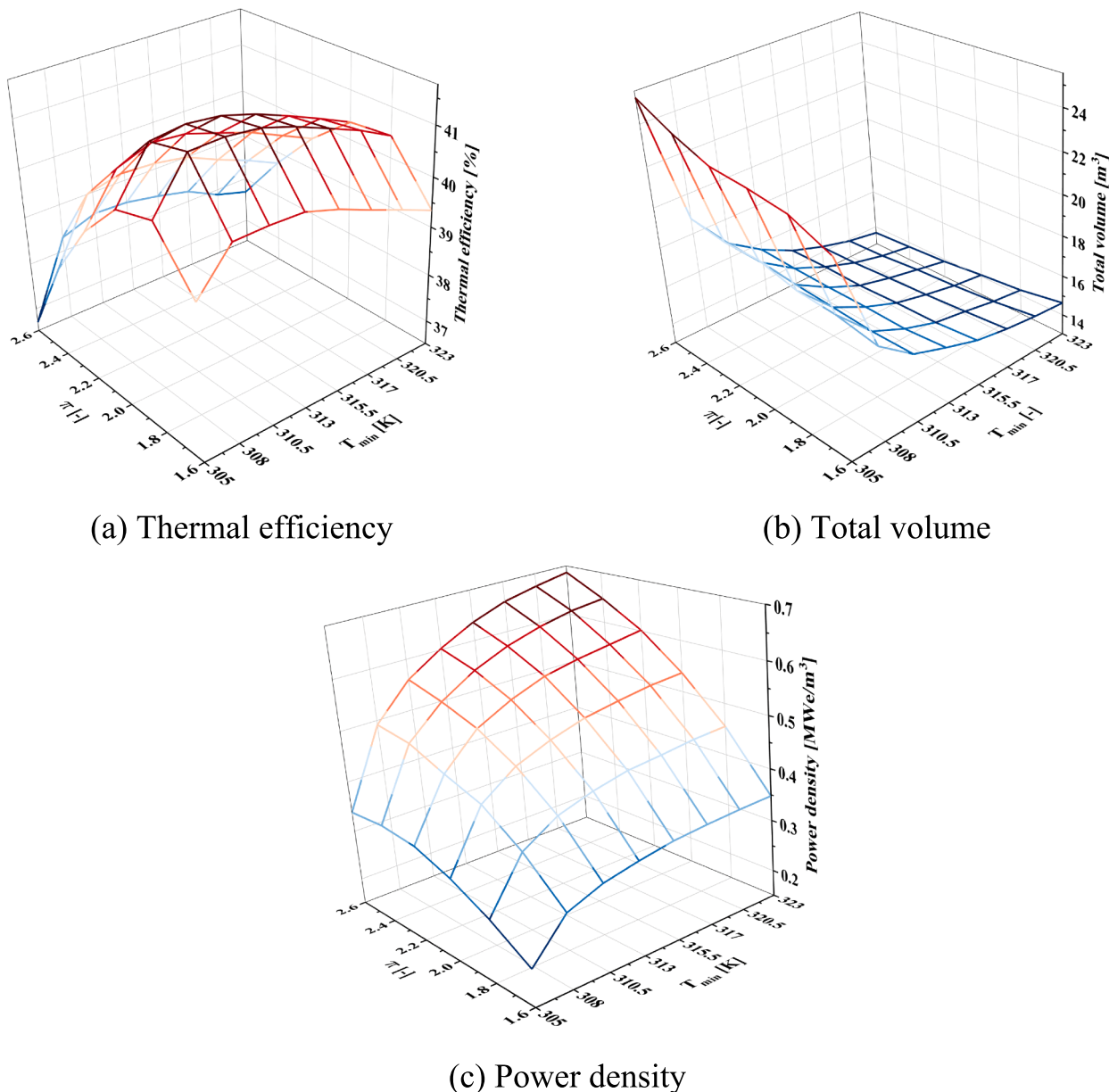


Fig. 19. Effects of compressor inlet temperature and pressure ratio.

precoolers of pure helium and 40 g/mol He-Xe, the HTC ranges on the air side are 136–148 $W/m^2/K$ and 119–129 $W/m^2/K$, respectively. This is because the cold-side flow area of the 15 g/mol He-Xe precooler is relatively small, resulting in a high air velocity. However, on the other hand, this also increases the pressure drop of the air flow as well as the fan power. The fan powers for precoolers of pure helium and 40 g/mol He-Xe are 224.47 kWe and 121.31 kWe, respectively, while for 15 g/mol He-Xe it is 466.55 kWe.

Table 11 and **Table 12** present the design results of the compressors and turbines, respectively. Because the compressor and turbine were arranged in a coaxial configuration, they were designed at the same rotation speed, which corresponds to a specific speed of 0.7 for the compressor. When the molecular weight increases, the specific enthalpy rise decreases in the compressor since the molar specific heat capacities of noble gases are nearly constant. As a result, the rotation speed decreases from 20,091 RPM of pure helium to 15,646 RPM of 40 g/mol He-Xe. Meanwhile, to limit the maximum tip speed below 500 m/s, a 5-stage turbomachinery was employed for pure helium. As a result, the maximum tip speed of the compressor is 485.37 m/s. A 2-stage design

was used for 15 g/mol He-Xe with a maximum tip speed of 399.31 m/s, and a single-stage design was employed for 40 g/mol He-Xe with a maximum tip speed of 385.58 m/s. The isentropic efficiencies of all turbines are above 90 %, while those of the compressors are around 83–87 %. As the molecular weight increases, the isentropic efficiency of the turbomachinery gradually increases, which contributes to the improved cycle efficiency.

Fig. 15 illustrates the efficiency decrement of components in the compressors and turbines. The stage losses are attributed to the isentropic head rise in the multi-stage compression. It can be observed that with increasing molecular weight of the He-Xe mixture, efficiency decrements of the rotor, stator, and stage decrease leading to higher machine efficiencies. For a specific He-Xe mixture, the efficiency decrement in the compressor stator is greater than that in the turbine. The distribution of losses in the compressor stator is depicted in **Fig. 16**. Frictional losses are predominant, followed by the losses of the upstream vaneless region (UVS) and downstream vaneless region (DVS). Frictional losses are influenced by the skin friction factor, blade length, hydraulic diameter, and fluid velocity. The Reynolds number at the stage inlet

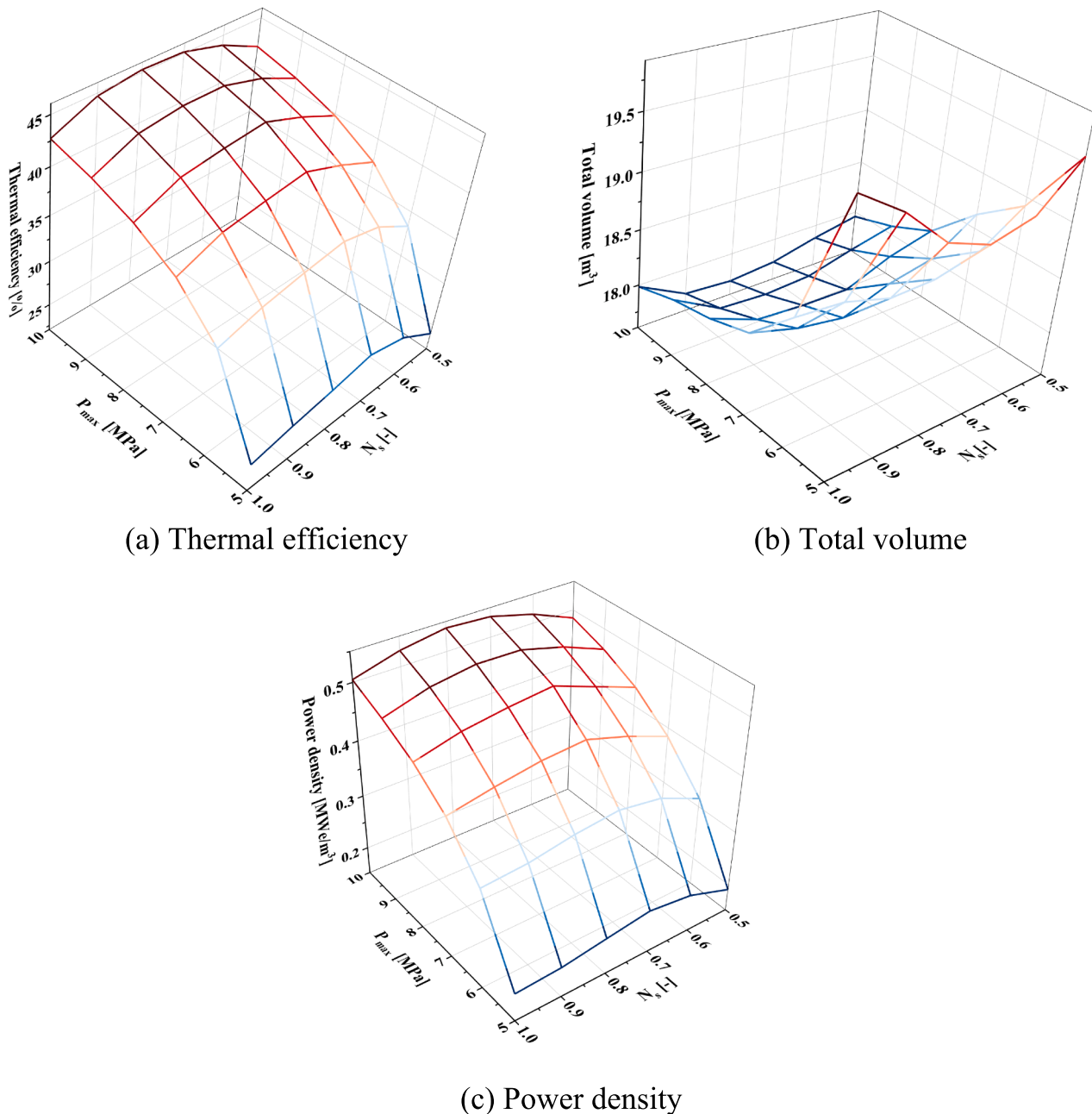


Fig. 20. Effects of compressor's specific speed and maximum cycle pressure.

increases from 1.27×10^8 of the pure helium to 4.21×10^8 of the 40 g/mol He-Xe, which brings a smaller skin friction factor. However, the increased stator blade number of the 40 g/mol compressor leads to a smaller hydraulic diameter. As a result, the friction loss of the 40 g/mol He-Xe increases slightly compared with that of the 15 g/mol He-Xe.

4.2. Performance of different He-Xe mixtures

Based on previous analysis, this section will further investigate the performances of different He-Xe mixtures in terms of system efficiency and volume. Apart from He-Xe's molecular weight, the other basic design parameters remained the same. The inlet Reynolds number of the heat exchanger was still selected by balancing the pressure drop and volume of the heat exchangers.

Fig. 17 depicts the changes in thermal efficiency from 4 g/mol helium to 40 g/mol He-Xe. The thermal efficiency demonstrates an

increasing trend with the growing molecular weight, climbing from 37.65 % of pure helium to 44.42 % of 40 g/mol He-Xe. Additionally, with the limitation of the maximum impeller tip speed, the turbomachinery is downsized to a single-stage configuration when the molecular weight is 20 g/mol or larger. It is observed that there is a slight reduction in the cycle efficiency at the molecular weight of 30 g/mol. This decrease is attributed to the increased pressure drop within the recuperator as displayed in Table 13. The relative pressure loss is calculated as the ratio of component pressure drop to the maximum cycle pressure, and the value of the recuperator is the sum of both the cold and hot sides. It can be seen that at the molecular weight of 30 g/mol, there is an increase in the pressure loss of the recuperator, 6.312 %, compared with 6.094 % of 25 g/mol. In other words, the inlet Reynolds number of 30 g/mol was selected at a large value with a high pressure loss when balancing the volume and pressure drop of the recuperator. In addition, the pressure loss within the reactor core gradually increases due to the

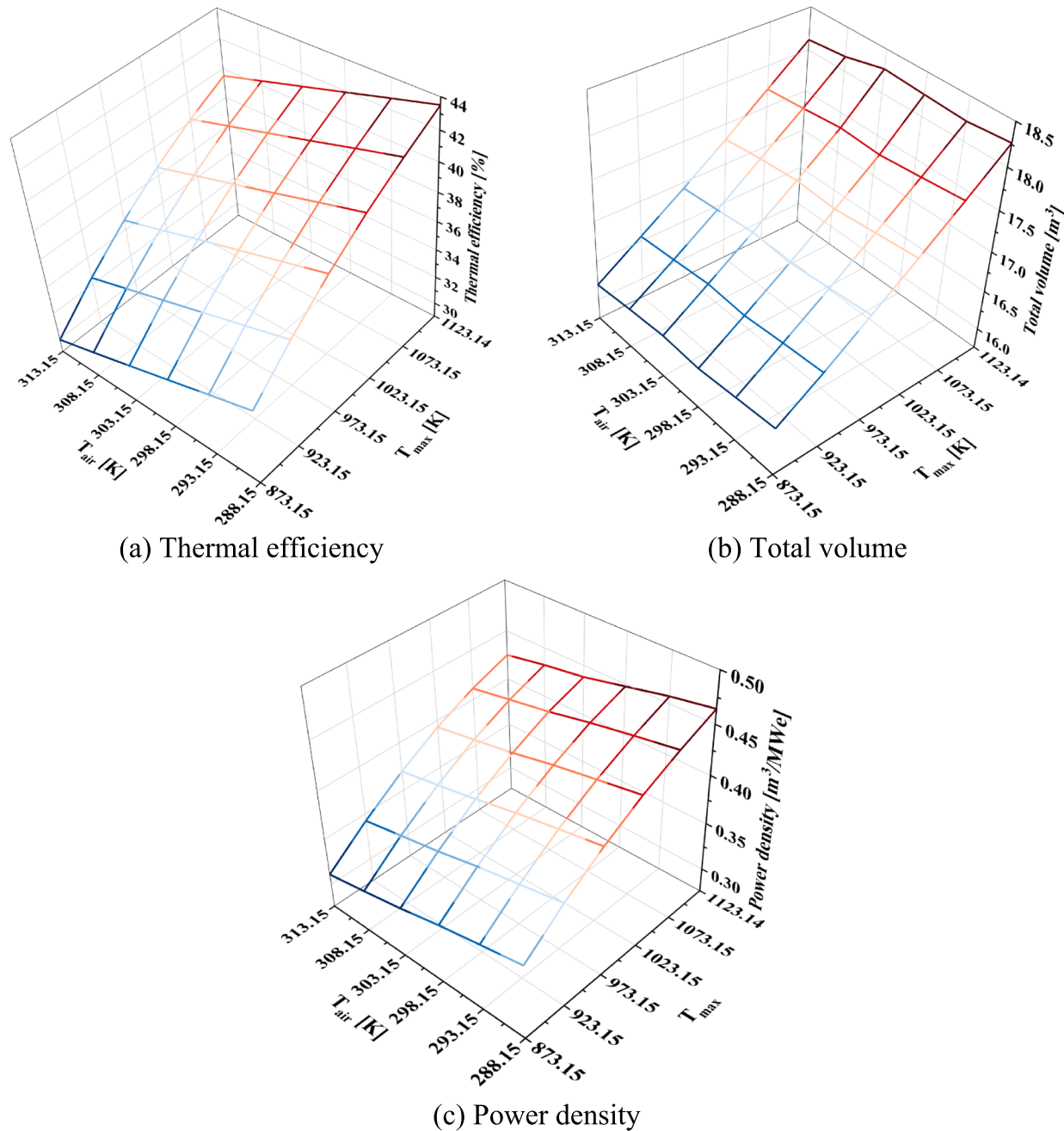


Fig. 21. Effects of cooling air temperature and maximum cycle temperature.

growing viscosity of the He-Xe mixture.

The increase in cycle efficiency does not necessarily imply a smaller system volume. Fig. 18 shows the variation of the total volume. In the range of 4–15 g/mol, the system volume decreases rapidly and it begins to increase when the molecular weight surpasses 30 g/mol. The detailed volumes of each component are presented in Table 14. Volumes of turbo-machinery and heat exchangers all decrease as the molecular weight increases from 4 g/mol to 15 g/mol. The reduction in turbo-machinery volume is attributed to decreased stage number and length. In terms of the heat exchanger, as the molecular weight increases, both the heat regeneration and heat rejection of the cycle decrease. For example, the heat regeneration and rejection of the cycle for the pure helium are 40.81 MW and 13.29 MW, respectively. They reduced to 37.94 MW and 12.36 MW for the 10 g/mol He-Xe cycle. The volume of the heat exchanger is influenced by the total heat transfer and HTC. When the molecular weight of He-Xe exceeds about 20 g/mol, the HTC

continues to decrease. The decrease in HTC slows down the rate of reduction in the heat exchanger volume, and eventually, the volume begins to increase. As a result, the total volume remains relatively low, at around 18.3 m³ when the molecular weight is between 15 g/mol and 30 g/mol, and further increasing the molecular weight brings a slight increase in the system volume.

Based on the analysis above, it is suggested to use a He-Xe mixture with a molecular weight ranging from 20 g/mol to 30 g/mol for the dry-cooled He-Xe Brayton cycle. This molecular weight range allows a small system volume. Moreover, when the molecular weight is greater than 20 g/mol, it is possible to employ a single-stage turbomachinery for the cycle. It is noted that the current results are based on the fluid properties of He-Xe. However, it is deduced that similar trends could also be obtained for other noble-gas binary mixtures such as He-Kr, considering the similarities in their thermodynamic and transport properties. What's more, the heat exchanger volume of He-Kr is supposed to be larger due

to a lower HTC compared with He-Xe [12].

4.3. Parametric analysis of crucial design parameters

In this section, a parametric analysis of design parameters was conducted, including the compressor's inlet temperature T_{min} , pressure ratio π , specific speed n_s , outlet pressure P_{max} , turbine inlet temperature T_{max} , and ambient air temperature T_{air} . The analysis focused on the previous design of 20 g/mol He-Xe.

Fig. 19 plots the impact of compressor inlet temperature and pressure ratio on cycle efficiency, system volume, and power density. During the calculation, the temperature of the ambient air was assumed to be constant at 303 K. The compressor's inlet temperature was varied from 305 K to 323 K, and the compressor's pressure ratio was varied from 1.6 to 2.6. It can be observed from **Fig. 19(a)** that the optimal pressure ratio for the cycle efficiency is between 1.8 and 2.0. As the pressure ratio increases, both the work of the compressor and turbine increase leading to a larger output power. However, the thermal power also increases. As the pressure ratio increases, the inlet temperature on the recuperator's cold side increases while that on the hot side decreases. With the $minTTD$ and mass flow rate fixed, the heat regeneration gradually decreases, causing the inlet temperature of the reactor core to drop and the thermal power to increase. Under the combined influence of the output power and thermal power, there is an optimal pressure ratio to maximize cycle efficiency.

When the pressure ratio remains constant, the compressor inlet temperature that yields the highest cycle efficiency is around 310.5 K. At this point, the change in the compressor inlet temperature affects the compression work and, through the change in pressure loss of the pre-cooler, influences the expansion ratio and work of the turbine. However, both changes are relatively small. For instance, at a pressure ratio of 1.6, an increase in compressor inlet temperature from 305 K to 323 K leads to a rise in compression work from 5.73 MW to 6.07 MW and a decrease in the relative pressure drop within the pre-cooler from 1.24 % to 0.17 %. Consequently, the expansion work of the turbine increases from 10.66 MW to 11.15 MW due to the growing expansion ratio.

The system volume gradually increases when the pressure ratio grows as depicted in **Fig. 19(b)**. Given that the geometric dimensions of the core remain unchanged, its volume is constant at 8.376 m³. The volumes of the compressors and turbines are relatively small, around 0.20 m³ and 0.50 m³, respectively. Therefore, the variation of the total volume is primarily influenced by the heat exchangers. As the pressure ratio grows, the recuperator volume gradually decreases due to the reduced heat regeneration, while the pre-cooler volume increases due to the increased heat rejection of the cycle. For example, at a compressor inlet temperature of 305 K, when the pressure ratio increases from 1.6 to 2.6, the volume of the pre-cooler increases from 8.54 m³ to 13.35 m³. Significant reduction in the pre-cooler volume can be achieved by increasing the compressor inlet temperature. For instance, the volume of the pre-cooler at a compressor inlet temperature of 323 K is only 1.07–2.13 m³, compared with 8.54–13.35 m³ at 305 K. What's more, the impact of compressor inlet temperature on cycle efficiency and output power is relatively small. Hence, higher power densities are achieved when the compressor inlet temperatures are higher as indicated in **Fig. 19(c)**.

Fig. 20 illustrates the influences of the compressor's specific speed and outlet pressure. The outlet pressure of the compressor also as the cycle's maximum pressure has a lowest value of 5 MPa. This is because when it is set at 4 MPa, the consumed power of the compressor will surpass the output power of the turbine due to the increased relative pressure loss. **Fig. 20(a)** reveals that the cycle's maximum pressure has a more pronounced effect on efficiency compared to the specific speed. As the P_{max} increases from 5 MPa to 10 MPa, the cycle efficiency increases from approximately 25 % to 42 %. The improvement in cycle efficiency mainly relies on the reduction of relative pressure drop within the heat exchangers. At a P_{max} of 5 MPa, the pressure losses within the

recuperator and the pre-cooler are 14.8 % and 2.2 %, respectively. Upon increasing the P_{max} to 10 MPa, these values decrease to 3.2 % and 0.57 %.

The system volume decreases from the range of 19.09–19.88 m³ to 17.73–17.98 m³ as the P_{max} is increased, which is shown in **Fig. 20(b)**. This is attributed to the volume changes of the compressor, turbine, and recuperator. As the pressure increases, the volume flow rates of the compressor and turbine decrease, resulting in smaller dimensions. At a P_{max} of 5 MPa, the volumes of the compressor and turbine are approximately 0.24–0.50 m³ and 0.84–1.5 m³, respectively. After increasing P_{max} to 10 MPa, these volumes decrease to approximately 0.09–0.19 m³ and 0.25–0.31 m³, respectively. Additionally, the volume of the recuperator also decreases from around 3.9 m³ to 3.3 m³ due to the reduced heat regeneration.

The impact of rotation speed on cycle efficiency is mainly through changes in turbomachinery efficiency. Since the compressor and turbine were assumed to be mounted on the same shaft, the variation in the compressor's specific speed implies a change in their rotation speed. As a result, the maximum cycle efficiency is achieved at a specific speed of 0.7. In terms of component volume, as the rotation speed increases, the compressor volume gradually decreases, but the turbine volume increases at larger rotation speeds. For example, at a P_{max} of 5 MPa, when the rotation speed increases from 14,359 RPM to 28,431 RPM, the turbine volume decreases from 0.94 m³ to 0.83 m³ and then increases to 1.50 m³. This is mainly due to the increased ratio of tangential velocity at the inlet to the outlet of the volute, resulting in a larger size of the inlet volute.

Fig. 21 illustrates the effects of cooling air temperature and maximum cycle temperature. The cooling air temperature varied from 288.15 K to 313.15 K, while the turbine inlet temperature ranged from 873.15 K to 1123.15 K. Meanwhile, the compressor inlet temperature was kept 5 K higher than the cooling air temperature. Therefore, as seen in **Fig. 21(a)**, when the air temperature decreases, the thermal efficiency approximately increases linearly due to the decline of the minimum cycle temperature. On the other hand, the heat duty of the pre-cooler also decreases resulting in a minor reduction in its volume. However, because of the growth of the recuperator volume, the system volume barely changes at different air temperatures, as shown in **Fig. 20(b)**. As a result, the system power density gradually increases as the air temperature decreases.

As for the maximum cycle temperature, which corresponds to the turbine inlet temperature, increasing its value can improve the cycle efficiency. However, due to the increased heat duty and volume of the recuperator, the total system volume also grows. For instance, when the turbine inlet temperature is 873.15 K, the heat duty of the recuperator ranges from 17.87 MW to 20.71 MW, with a volume range of 1.59–1.81 m³. When the turbine inlet temperature rises to 1123.15 K, the heat duty of the recuperator increases to 35.35 MW–38.15 MW, with a volume range of 3.42 m³–3.64 m³. Overall, after increasing the maximum cycle temperature, the growth rate of output power is larger than that of the system volume. Hence, the maximum power density occurs at the design point corresponding to the highest cycle temperature and lowest air temperature.

Based on the analysis above, it is identified that increasing the compressor's inlet temperature and outlet pressure are the main measures to consider for reducing the system volume. Moreover, the influence of the compressor's pressure ratio on system volume depends on the heat exchangers, while the influence of specific speed on system volume is mainly through the turbine under a TAC configuration.

5. Conclusion

In the current study, an integrated design approach for the dry-cooled Brayton cycle was proposed based on detailed models of the cycle components. With this method, the 8 MWe designs of pure helium, 15 g/mol, and 40 g/mol He-Xe were established and detailed results of

the cycle components were demonstrated. Furthermore, the performance of using different He-Xe mixtures and the effects of some key design parameters were discussed. The following deductions were made based on the findings in the aforementioned sections.

- (1) (1). Although the turbomachinery occupies a rather smaller volume compared with the reactor core and heat exchanger, the inlet temperature of the compressor significantly affects the system volume through that change of the precooler. Additionally, a smaller pressure loss can be obtained with a larger molecular weight of He-Xe when selecting the cross-section of the heat exchanger by balancing its volume and pressure drop.
- (2) (2). In contrast to the previous results obtained from simplified component models, it is found that increasing the molecular weight of the He-Xe mixture could improve the cycle efficiency due to the increasing efficiency of the turbomachinery and reduction of the pressure loss in the heat exchanger. He-Xe mixtures of 20–30 g/mol are recommended for a nuclear micro-reactor system as they bring smaller system volumes. Besides, the

single-stage turbomachinery can be used when the molecular weight of He-Xe exceeds 20 g/mol.

- (3) (3). Raising the compressor's inlet temperature could significantly reduce the volume of the precooler, and the decrease in cycle efficiency is small. When designing the compressor and the turbine at the same rotation speed, the optimal pressure ratio for thermal efficiency is between 1.8 and 2.0, and the optimal specific speed of the compressor is around 0.7.

Declaration of competing interest

The authors declare that they have no known competing financial interests or personal relationships that could have appeared to influence the work reported in this paper.

Acknowledgments

This work is supported by the National Key R&D Program of China (2020YFB1901900).

Appendix A. . Empirical correlations for the preliminary design of the heat exchanger

The Nusselt number calculation of the He-Xe mixture referred to the work of Dragunov et al [33]. Specifically, (18)~(20) were used,

$$Nu = 4.364 + \frac{0.2633}{\left(\frac{1}{Pe} \frac{L}{d}\right)^{0.506}} \exp\left(41 \frac{1}{Pe} \frac{L}{d}\right), \quad Re < 2300 \quad (18)$$

$$Nu = (1 - \gamma)Nu_l + \gamma Nu_t, \quad 2300 < Re < 10^4 \quad (19)$$

$$Nu = Nu_0 (T_w/T_b)^n, \quad 10^4 < Re < 5 \times 10^6$$

$$Nu_0 = \frac{Re Pr(f/8)}{1.07 + 12.7(Pr^{2/3} - 1)\sqrt{f/8}} \quad (20)$$

$$n = a \log_{10}(T_w/T_b)^b + c$$

$$f = (1.82 \log_{10} Re - 1.64)^{-2}$$

where $Pe = Lu/\alpha$ is the Peclet number, α is the thermal diffusion coefficient, Nu_l is the Nusselt number calculated at $Re = 2300$, Nu_t is the Nusselt number calculated at $Re = 10^4$, $\gamma = (Re - 2300)/(10^4 - 2300)$, $a = 0$, $c = -0.36$ for the case of gas cooling, $a = -1$, $b = 0.25$, $c = 0.3$ for gas heating.

For the friction factor calculation of the He-Xe mixture, the Colebrook-white correlations were used. Specifically, Eq. (21) was used for the laminar flow and Eq. (22) was used for the fully turbulent flow ($Re > 4000$).

$$f = \frac{64}{Re} \quad (21)$$

$$\frac{1}{\sqrt{f}} = -2.0 \log_{10}\left(\frac{\epsilon/D_h}{3.7} + \frac{2.51}{Re\sqrt{f}}\right) \quad (22)$$

As for the cold side of the precooler where the working fluid is air, correlations for the Nusselt number and friction factor were referenced from the work of Moisseytsev & Sienicki [35]. Specifically, for the Nusselt number, Eq. (23) was used,

$$Nu = j \cdot Re \cdot Pr^{1/3} \quad (23)$$

where j is the Colburn factor. In the turbulent region ($Re > 2300$),

$$j_{turb} = 0.1341 a_j \cdot Re^{-0.3319}; \quad a_j = 0.6 + \tan(\alpha/2) \quad (24)$$

where α is the channel angle. In the laminar region ($Re < 2300$), the Colburn factor for a zigzag channel is defined as an enhancement over the straight channel,

$$j_{0,lam} = 4.1/Re \quad (25)$$

$$(j/j_0)_{lam} = 1 + a_{j,lam}(Re + 50)$$

where is defined from the continuity of the heat transfer correlation as

$$a_{j,\text{lam}} = \frac{a_j 0.1341 \cdot (1300)^{-0.3319} \cdot \frac{1300}{4.1} - 1}{1300 + 50} \quad (26)$$

For the friction factor, Eq. (27) was used,

$$f/f_0 = \begin{cases} 1 + a_f(Re + 50), & Re < 1300 \\ kRe^c, & Re \geq 1300 \end{cases} \quad (27)$$

where f_0 is the friction factor through a straight channel, defined as Eq. (28), together with a simple linear function in the transition region ($1700 < Re < 2300$),

$$f_0 = \begin{cases} 64/Re, & Re < 1700 \\ 0.3164/Re, & Re > 2300 \end{cases} \quad (28)$$

The coefficients, k , c , and a_f , were found from curve fitting from the Argonne's PCHE experiment:

$$\begin{aligned} c &= \frac{\ln\left(\frac{1 + 223283a_f^2}{1 + a_f(1300 + 50)}\right)}{\ln\left(\frac{100,000}{1300}\right)}; \\ k &= \frac{1 + a_f(1300 + 50)}{1300^c}; \\ a_f &= 4.5 \times 10^{-3} \tan(\alpha/2) \end{aligned} \quad (29)$$

Appendix B. . Component sizing method and loss models for the turbomachinery preliminary design

For the centrifugal compressor, the isentropic enthalpy rise was determined by $\Delta h_{is}^* = h(P_6^*, s_1^*) - h_1^*$. With rotation speed evaluated from input specific speed, the runner inlet hub radius r_{1h} was obtained based on the material limitation using Eq. (30) to ensure the gross torque is below the shear stress limit of the material. The inlet tip radius r_{1t} was obtained using the Min-Relative-Tip-Mach method by adjusting the C_{m1} to achieve the optimal relative flow angle β_1 [40]. Specifically, with a value of C_{m1} , the inlet static enthalpy was determined $h_1 = h_1^* - 0.5C_{m1}^2$, resulting in the inlet density. Then the tip radius was estimated based on the mass continuity, and the velocity triangle at the middle-passage was established. An optimal β_1 can be found resulting in the minimum $Ma_{1t,\text{rel}}$ estimated from the free vortex equation when increasing the C_{m1} . The runner blade number was calculated using Eq. (31) [4142]. The radii of the runner inlet The inlet blade angle β_{1b} was set equal to the relative inflow angle with zero incidence assumed.

$$r = \frac{1}{2} \left(\frac{16P}{\omega \pi \tau_{int}} \right)^{1/3} \quad (30)$$

$$Z_{RN} = \text{int}(12.03 + 2.544\pi_{it}) \quad (31)$$

The **runner** outlet rotating speed U_2 was obtained by the loading coefficient $U_2 = \sqrt{\Delta h_{is}^*/\psi_{is}}$, and the outlet tangential velocity C_{U2} was obtained by the Euler equation, Eq. (32). The outlet triangle was established with a specified absolute angle α_2 (generally $65^\circ \sim 75^\circ$). The outlet blade angle β_{2b} was iteratively calculated using Eq. (33)~(34), where ΔC_{U2} was estimated using the flow slip model proposed by Wiesner [43].

$$\Delta(UC_U) = \Delta h^* \quad (32)$$

$$\beta_{2b} = \tan^{-1} \left(\frac{W_{U2} - \Delta C_{U2}}{W_{m2}} \right) \quad (33)$$

$$\sigma = 1 - \frac{\Delta C_{U2}}{U_2} = 1 - \frac{\sqrt{\cos \beta_{2b}}}{Z_{RN}^{0.7}} \quad (34)$$

An isentropic compression was assumed in the **vaned diffuser**. The blade number of the vaned diffuser was $Z_{VD} = (1.0 \sim 1.3)Z_{RN}$. The radius r_3 was iteratively calculated using Eq. (35). The velocity triangle at the diffuser inlet was established by applying angular momentum conservation and mass continuity. The inlet blade angle β_{3b} was set equal to the inflow angle α_3 at the inlet of the diffuser. The exit blade angle β_{4b} and outlet flow angle α_4 were calculated using Eq. (36) and (37) [3844].

$$r_3 = r_2 \left(1 + \frac{90 - \alpha_3}{360} + \frac{Ma_2^2}{15} \right) \quad (35)$$

$$\frac{\cos \beta_{3b}}{\cos \beta_{4b}} = \sqrt{\frac{3 - (r_4/r_3)^2}{2}} \quad (36)$$

$$\alpha_4 = \beta_{4b} - \delta^* - \frac{\partial \delta}{\partial t} (\beta_{3b} - \alpha_3) \quad (37)$$

An external volute with a round cross-section was adopted in the current study. The dimensions and flow conditions from the diffuser outlet were used as boundary conditions. The aspect ratio $AR = L_A/L_B$ and sizing $SP = r_5 C_{U5}/(r_6 C_6)$ parameters were specified as design parameters. Flow losses within the volute were neglected during the design process. The dimensions and velocity at station 6 were iteratively determined by solving mass continuity [38].

For the **radial turbine**, the design process was similar. The rotation speed at the runner inlet was determined based on the isentropic loading coefficient ψ_{is} . With the runner outlet axial spouting assumption ($C_{6U} = 0$), the inlet tangential velocity C_{5U} was obtained by the Euler equation. The absolute flow angle α_5 was estimated using Eq. (38), and the runner inlet velocity triangle was established.

$$\alpha_5 = 90 - [10.8 + 14.2(2\pi N_s)^2] \quad (38)$$

The inlet radius was $r_5 = U_5/\omega$, and the blade height b_5 was calculated based on mass continuity as shown in Eq. (39), and the blockage factor was calculated using Eq. (40). The zero runner inlet blade angle ($\beta_{5b} = 0$) was adopted. The runner blade number was calculated using Eq. (41) [45]

$$b_5 = \frac{\dot{m}}{2\pi r_5 \rho_5 C_{5m}(1-B_5)} \quad (39)$$

$$B_5 = \frac{t_b Z_{RN}}{2\pi r_5 \cos \beta_{5b}} \quad (40)$$

$$Z_{RN} = \text{int}\left[\frac{\pi}{30}(20 + \alpha_5)\tan(90 - \alpha_5)\right] \quad (41)$$

The runner outlet hub radius r_{6h} was obtained based on material stress limitation, and the outlet velocity triangle was established using the Min-Relative-Tip-Mach method. The runner outlet tip radius r_{6t} was obtained from mass continuity. The outlet blade angle β_{6b} was obtained based on the deviation model given by Eq. (42) [4647].

$$\frac{90 - \beta_6}{90 - \beta_{6b}} = 1 + \frac{3\pi}{Z_{RN}} \left(\frac{\dot{m} \sqrt{RT_1^*}}{4r_5^2 \rho_6 a_1} \right)^{a_2} + 7.85 \frac{\varepsilon_r}{r_{6t} - r_{6h}} \quad (42)$$

where $a_1 = 2\tan(90 - \beta_{6b}) - 0.5$, and $a_2 = 0.02\tan(90 - \beta_{6b}) - 0.255$

The **nozzle** was designed from the outlet to the inlet with boundary conditions obtained from the runner inlet. The blade height was equal to the runner inlet ($b_3 = b_5$). The outlet radius of the nozzle was obtained as $r_4 = r_5 + b_5 \cos \alpha_5$. The velocity triangle at the nozzle inlet was established using mass continuity and angular momentum conservation. The exit blade angle β_{4b} was iteratively calculated using Eq. (44), where the blade pitch $p_4 = 2\pi r_4/Z_{NZ}$ and the throat width is $o_4 = (p_4 - t_{b4}) \cos \beta_{4b}$

$$C_{4U} r_4 = C_{5U} r_5 \quad (43)$$

$$\alpha_4 = \begin{cases} 4.3 + 0.96 \cos^{-1}(o_4/p_4), & Ma_4 < 0.3 \\ 4.3 + 0.96 \cos^{-1}(o_4/p_4) - 3.2(Ma_4 - 0.3), & Ma_4 > 0.3 \end{cases} \quad (44)$$

The nozzle inlet radius r_3 was determined according to the radius ratio r_3/r_4 . The optimal inlet absolute flow angle α_{3opt} was calculated using Eq. (45), where i_{opt} is the optimal incidence angle.

$$\alpha_{3, opt} = \beta_{3b} + i_{opt} \text{sign}(\beta_{3b} - \beta_{4b}) \quad (45)$$

$$i_{opt} = (3.6 \sqrt{\frac{10t_{b3}}{L_{cam}}} + \frac{|\beta_{3b} - \beta_{4b}|}{3.4}) \sqrt{\frac{L_{cam}}{p_4}} - 0.5 |\beta_{3b} - \beta_{4b}| \quad (46)$$

Table 15

Loss models for the compressor analysis [2438].

Centrifugal compressor**Runner**

Incidence loss

$$\Delta h_{inc,RN}^* = \frac{W_1^2}{24} (\bar{\omega}_{hub} + \bar{\omega}_{mid} + \bar{\omega}_{tip})$$

$$\bar{\omega} = 0.8 \left(1 - \frac{C_{m,1}}{W_1 \cos \beta_{b,1}} \right)^2 + \left(\frac{Z_{RN} t_{b,1}}{2\pi r_1 \cos \beta_{b,1}} \right)^2$$

Skin friction loss

$$\Delta h_{fric,RN}^* = 2c_f \frac{L_h}{d_h} \frac{(W_1^2 + W_2^2)}{2}$$

$$L_h = 0.25\pi [2r_2 - (r_{1t} + r_{1h}) - b_2 + 2L_a] [0.5(\cos \beta_{b,1h} + \cos \beta_{b,1t}) + \cos \beta_{b,2}]^{-1}$$

$$d_h = \frac{2r_2}{Z/(\pi \cos \beta_{b,2}) + 2r_2/b_2} + \frac{2r_{1t}}{2/(1-\lambda) + \sqrt{1 + (1 + \lambda^2/2) \tan^2(\beta_{b,1t}) 2Z/(\pi + \pi\lambda)}} \\ \lambda = \frac{r_{1h}}{r_{1t}}$$

Blade loading loss

$$\Delta h_{ld,RN}^* = \frac{\Delta W^2}{48} + \frac{(\bar{\kappa}_m \bar{b} \bar{W})^2}{12}$$

$$\Delta W = \frac{2\pi d_2 U_2 I_b}{Z L_b}$$

$$I_b = (U_2 C_{u,2} - U_1 C_{u,1}) U_2^2$$

$$\bar{k}_m = \frac{|\alpha_{C2} - \alpha_{C1}|}{L_b}, \bar{b} = (b_1 + b_2)/2$$

$$\bar{W} = (W_1 + W_2)/2$$

Distortion loss

$$\Delta h_{dist,RN}^* = 0.5 \left(\frac{1}{1 - B_2} - 1 \right)^2 C_{m,2}^2$$

Mixing loss

$$\Delta h_{mix,RN}^* = 0.5(C_{m,wake} - C_{m,mix})^2$$

$$C_{m,mix} = C_{m,2} A_2 / (\pi d_2 b_2)$$

$$C_{m,wake} = \begin{cases} \sqrt{W_{sep}^2 - W_{U2}^2}, & W_{sep} > |W_{U2}| \\ C_{m,mix}, & W_{sep} \leq |W_{U2}| \end{cases}$$

$$W_{sep} = \begin{cases} W_2 D_{eq}/2, & D_{sep} > 2 \\ W_2, & D_{sep} \leq 2 \end{cases}$$

$$D_{eq} = W_{max}/W_2$$

$$W_{max} = (W_1 + W_2 + \Delta W)/2$$

Disk friction loss

$$\Delta h_{disk}^* = (C_{M,front} + C_{M,rear}) \rho_2 U_2^3 r_2^2 / (2 \dot{m})$$

$$C_{M,rear} = 0.5 C_M$$

$$C_{M,front} = (0.75 L_m C_M) / (r_{s2} - r_{s1})$$

$$C_M = C_{Ms} + (C_{Mr} - C_{Ms}) \frac{\log(\text{Re}/\text{Re}_s)}{\log(\text{Re}_r/\text{Re}_s)}$$

$$\text{Re}_r = 1100 r_2 / e - 6 \times 10^6$$

$$\text{Re}_s = 1100 (e/r_2)^{-0.4} / \sqrt{C_{Ms,2}}$$

$$1/\sqrt{C_{Mr}} = 3.0 \log(r_2/e) - 2.4 (\epsilon_b/r_2)^{0.25}$$

$$C_{Ms} = \max(C_{Ms,1}, C_{Ms,2}),$$

$$C_{Ms,1} = \max(C_{M,1}, C_{M,2})$$

$$C_{M,1} = \frac{2\pi}{\text{Re}(\epsilon_b/r_2)}, \quad C_{M,2} = \frac{3.7(\epsilon_b/r_2)^{0.1}}{\sqrt{\text{Re}}}$$

$$C_{M,3} = \frac{0.08}{\text{Re}^{0.25} (\epsilon_b/r_2)^{1/6}}, \quad C_{M,2} = \frac{0.102(\epsilon_b/r_2)^{0.1}}{\text{Re}^{0.2}}$$

$$\text{Re} = \rho \omega r_2^2 / \mu$$

Table 15 (continued)**Centrifugal compressor****Vaned diffuser**

Incidence loss

$$\Delta h_{inc,VD}^* = \Delta h_{ml} + \Delta h_{od}$$

$$\Delta h_{ml} = 0.4(C_3^* - C_{th3})^2 + \frac{Z \cdot t_{b,3}}{(2\pi r_3)} C_1^2$$

$$\cos \alpha_{3,opt} = \frac{C_{m,3}}{C_{3,opt}} = \sqrt{\cos \beta_{3b} \cos \alpha_{th3}}$$

$$\alpha_{th3} = \arccos(A_{th3}/A_3)$$

$$\Delta h_{od} = \begin{cases} 0.4(C_3 - C_{3,opt})^2, & C_3 \leq C_s \\ 0.4 \{ [(C_3/C_s)^2 - 1] C_{th3}^2 + (C_s - C_{3,opt})^2 / C_s^2 \} & \end{cases}$$

$$C_s = C_{m,3} / \cos \alpha_{3s}$$

$$\alpha_{s,3} = \sin^{-1} \{ \sin \alpha_{th3} [1.0 + (0.39 - K_0) o_3 / r_3] \}$$

$$K_0 = \frac{(Ma_3 \cos \beta_{b,3})^2 \sin \beta_{b,3}}{1 - (Ma_3 \cos \beta_{b,3})^2}$$

$$o_3 = 2\pi r_3 \cos \beta_{b,3} / Z - t_{b,3}$$

Skin friction loss

Same with the runner but using absolute velocity.

Blade loading loss

Same with the runner but using absolute velocity.

Distortion loss

Same with the runner but using absolute velocity.

Wake mixing loss

$$\Delta h_{mix,VD}^* = 0.5(C_{m,wake} - C_{m,mix})^2$$

$$C_{m,mix} = C_{m,4} A_4 / (\pi d_4 b_4)$$

$$C_{m,wake} = \begin{cases} \sqrt{W_{sep}^2 - C_{U2}^2}, & C_{sep} > C_{U4} \\ C_{m,mix}, & C_{sep} \leq C_{U4} \end{cases}$$

$$C_{sep} = \min[C_3 / (1 + 2C_g), C_4]$$

Vaneless space skin friction loss

$$\Delta h_{fric,VS}^* = 2c_f \frac{L_h}{d_h} \frac{(C_2^2 + C_3^2)}{2}$$

$$L_h = (r_3 - r_2) / \cos \bar{\alpha}, \quad \bar{\alpha} = 0.5(\alpha_2 + \alpha_3)$$

$$d_h = (b_2 + b_3) \cos \bar{\alpha}$$

Volute

Tangential velocity dump loss

$$\Delta h_{tv,VT}^* = \bar{\omega}_U C_5^2 / 2$$

$$\bar{\omega}_U = \begin{cases} \frac{1}{2} \frac{r_5 C_{U5}^2}{r_6 C_5^2} [1 - \frac{1}{SP^2}], & SP \geq 1 \\ \frac{r_5 C_{U5}^2}{r_6 C_5^2} [1 - \frac{1}{SP}]^2, & SP < 1 \end{cases}$$

$$SP = r_5 C_{U5} / (C_6 r_6)$$

Skin friction loss

$$\Delta h_{fric,VR}^* = 2c_f \frac{L_h}{d_h} C_6^2$$

$$L_h = \pi(r_5 + r_6)/2$$

$$d_h = \sqrt{4A_6/\pi}$$

Table 16
Loss models for the turbine analysis [24,38].

Radial turbine	
Runner	
Incidence loss	
$\Delta h_{inc,RN}^*$	$= \frac{W_5^2}{2} \sin^n(\beta_5 - \beta_{5,opt})$
$\beta_{5,opt}$	$= \tan^{-1}(\frac{-1.98 \tan \alpha_5}{Z(1-1.98/Z)})$
n	$= \begin{cases} 2, & \beta_5 < \beta_{5,opt} \\ 3, & \beta_5 > \beta_{5,opt} \end{cases}$
Passage Loss	
$\Delta h_{psg,RN}^*$	$= K_p \left\{ \frac{L_h}{d_h} + 0.68 \left[1 - \left(\frac{r_6}{r_5} \right)^2 \right] \left(\frac{\cos \beta_{b6}}{b_6/c_{RN}} \right) \right\} \frac{W_5^2 + W_6^2}{2}$
K_p	$= \begin{cases} 0.11, & (r_5 - r_{6t})/b_6 \geq 0.2 \\ 0.22, & (r_5 - r_{6t})/b_6 < 0.2 \end{cases}$
L_h	$= \frac{\pi}{4} \left[(L_a - \frac{b_5}{2}) + (r_5 - r_{6t} - \frac{b_6}{2}) \right]$
d_h	$= \frac{2\pi r_5 b_5}{2\pi r_5 + Zb_5} + \frac{\pi(r_{6t}^2 - r_{6h}^2)}{\pi(r_{6t} - r_{6h}) + Zb_6}$
c_{RN}	$= L_a / \cos \bar{\beta}, \tan \bar{\beta} = 0.5(\tan \beta_{b5} + \tan \beta_{b6})$
Trailing edge loss	
$\Delta h_{te,RN}^*$	$= 0.5 W_6^2 (\frac{Z b_6}{2\pi 4_6 \cos \beta_6})^2 Y_6$
Y_6	$= (1 + \frac{k_6 - 1}{2} Ma_{6,rel}^2)^{k_6/(1-k_6)}$
Disk friction loss	
Δh_{disk}^*	$= [K_{df}(\rho_5 + \rho_6) U_5^2 r_5^2] / (8\dot{m})$
K_{df}	$= \begin{cases} 3.7(\epsilon_b/b_5)^{0.1} Re_5^{-0.5}, & Re_5 < 3 \times 10^5 \\ 0.102(\epsilon_b/b_5)^{0.1} Re_5^{-0.2}, & Re_5 > 3 \times 10^5 \end{cases}$
Re_5	$= \rho_5 U_5 r_5 / \mu_5$
Nozzle	
Incidence loss	
$\Delta h_{inc,NZ}^*$	$= 0.5 C_3^2 \sin^2(\alpha_3 - \alpha_{3,opt})$
$\alpha_{3,opt}$	$= \beta_{b3} + i_{opt} \text{sign}(\beta_{b3} - \beta_{b4})$
i_{opt}	$= (2.6 \sqrt{10 t_{b3}/L_b} + \beta_{b3} - \beta_{b4} /3.4) \sqrt{L_b/p_4} - \beta_{b3} - \beta_{b4} /2$
Passage	
$\Delta h_{psg,NZ}^*$	$= 2c_f \frac{L_h}{d_h b_{corr}^{0.25}} \left(\frac{C_1 + C_2}{2} \right)^2$
b_{corr}	$= \frac{5.142 c_f L_h}{d_h}$
L_h	$= (r_3 - r_4) / \cos(\beta_{b3} + \beta_{b4})$
d_h	$= o_3 b_3 / (o_3 + b_3) + o_4 b_4 / (o_4 + b_4)$
Trailing edge loss	
Same with the runner but using absolute velocity.	
Vaneless space skin friction loss	
$\Delta h_{fric,VS}^*$	$= 2c_f \frac{L_h}{d_h} \frac{(C_2^2 + C_3^2)}{2}$
L_h	$= (r_2 - r_3) / \cos \bar{\alpha}, \bar{\alpha} = 0.5(\alpha_2 + \alpha_3)$
d_h	$= (b_2 + b_3) \cos \bar{\alpha}$
Inlet volute	
Tangential velocity dump loss	
$\Delta h_{tv,VT}^*$	$= \bar{\omega}_U C_2^2 / 2$
$\bar{\omega}_U$	$= \begin{cases} \frac{1}{2} \frac{r_2 C_{U2}^2}{r_1 C_1^2} [1 - \frac{1}{SP^2}], & SP \geq 1 \\ \frac{r_2 C_{U2}^2}{r_1 C_1^2} [1 - \frac{1}{SP}]^2, & SP < 1 \end{cases}$
SP	$= r_2 C_{U2} / (C_1 r_1)$
Skin friction loss	
$\Delta h_{fric,VT}^*$	$= 2c_f \frac{L_h}{d_h} C_1^2$
L_h	$= \pi(r_1 + r_2) / 2$
d_h	$= \sqrt{4A_1/\pi}$

Data availability

Data will be made available on request.

References

- [1] A. Chaube, Z. Ahmed, B. Sieh, C.S. Brooks, H. Bindra, Nuclear microreactors and thermal integration with hydrogen generation processes, *Nucl. Eng. Des.* 419 (2024) 112968, <https://doi.org/10.1016/j.nucengdes.2024.112968>.
- [2] G. Black, D. Shropshire, K. Araújo, A. van Heek, Prospects for nuclear microreactors: A review of the technology, economics, and regulatory considerations, *Nucl. Technol.* 209 (supl) (2023) S1–S20, <https://doi.org/10.1080/00295450.2022.2118626>.
- [3] R. Testoni, A. Bersano, S. Segantini, Review of nuclear microreactors: Status, potentialities and challenges, *Prog. Nucl. Energy* 138 (2021) 103822, <https://doi.org/10.1016/j.pnucene.2021.103822>.
- [4] X Energy LLC, Reactor: Xe-Mobile. <https://x-energy.com/reactors/xe-mobile/>, 2024, (accessed 21 July 2024).
- [5] E. Nygaard, BWXT's advanced nuclear reactor. <https://www.nationalacademies.org/event/01-11-2021/docs/DD7F72C500641846CD3FC86C8D19F97B8889C926B7DE>, 2024, (accessed 21 July 2024).
- [6] Holos Gen LLC, From turbo-jet engines to Holos generators. <https://www.holosgen.com/generators/>, 2024, (accessed 21 July 2024).
- [7] URESCO, U-Battery A Future Energy Solution. https://www.u-battery.com/cdn/uploads/supporting-files/U-Battery_brochure_Feb21.pdf, 2024, (accessed 21 July 2024).
- [8] Radiant Industries Inc., Kaleidos A Portable Nuclear Microreactor that Replace Diesel Generators. <https://radiantnuclear.com/>, 2024, (accessed 21 July 2024).
- [9] Ultra Safe Nuclear, MMR Energy System Micro Modular Reactor. <https://www.usnc.com/mmr/>, 2024, (accessed 21 July 2024).
- [10] NuGen LLC, Mission: Develop an Innovative Fully Integrated Microreactor. <https://www.nucdev.com/>, 2024, (accessed 21 July 2024).
- [11] P. Xiang, K. Jiang, J. Wang, C. He, S. Chen, W. Jiang, Evaluation of LCOH of conventional technology, energy storage coupled solar PV electrolysis, and HTGR in China, *Appl. Energy* 353 (2024) 122086, <https://doi.org/10.1016/j.apenergy.2023.122086>.
- [12] M.S. El-Genk, J.M. Tournier, On the use of noble gases and binary mixtures as reactor coolants and CBC working fluids, *Energ. Convers. Manage.* 49 (2008) 1882–1891, <https://doi.org/10.1016/j.enconman.2007.08.017>.
- [13] J. Ashcroft, C. Eshelman, Summary of NR program Prometheus efforts, *AIP Conf. Proc.* 880 (2007) 497–521, <https://doi.org/10.1063/1.2437490>.
- [14] Z. Li, J. Sun, M. Liu, M. Lang, L. Shi, Design of a hundred-kilowatt level integrated gas-cooled space nuclear reactor for deep space application, *Nucl. Eng. Des.* 361 (2020) 110569, <https://doi.org/10.1016/j.nucengdes.2020.110569>.
- [15] S.G. Kim, H. Yu, J. Moon, S. Baik, Y. Kim, Y.H. Jeong, J.I. Lee, A concept design of supercritical CO₂ cooled SMR operating at isolated microgrid region, *Int. J. Energy Res.* 41 (2017) 512–525, <https://doi.org/10.1002/er.3633>.
- [16] A. Moisseytsev, J.J. Sienicki, Q. Lv, Dry Air Cooler Modeling for Supercritical Carbon Dioxide Brayton Cycle Analysis, United States (2016), <https://doi.org/10.2172/1342159>.
- [17] B. Sondelski, G. Nellis, Mass optimization of a supercritical CO₂ Brayton cycle with a direct cooled nuclear reactor for space surface power, *Appl. Therm. Eng.* 163 (2019) 114299, <https://doi.org/10.1016/j.applthermaleng.2019.114299>.
- [18] X. Miao, H. Zhang, W. Sun, Q. Wang, C. Zhang, Optimization of a recompression supercritical nitrous oxide and helium Brayton cycle for space nuclear system, *Energy* 242 (2022) 123023, <https://doi.org/10.1016/j.energy.2021.123023>.
- [19] D. Luo, D. Huang, Thermodynamic and exergoeconomic investigation of various CO₂ Brayton cycles for next generation nuclear reactors, *Energ. Convers. Manage.* 209 (2020) 112649, <https://doi.org/10.1016/j.enconman.2020.112649>.
- [20] Z. Rao, T. Xue, K. Huang, S. Liao, Multi-objective optimization of supercritical carbon dioxide recompression Brayton cycle considering printed circuit recuperator design, *Energ. Convers. Manage.* 201 (2019) 112094, <https://doi.org/10.1016/j.enconman.2019.112094>.
- [21] H. Liu, Z. Chi, S. Zang, Optimization of a closed Brayton cycle for space power systems, *Appl. Therm. Eng.* 179 (2020) 115611, <https://doi.org/10.1016/j.applthermaleng.2020.115611>.
- [22] Y. Du, L. Wang, Z. Yu, H. Zhang, Y. Li, C. Yang, Multi-objective optimization of thermoeconomic and component size of supercritical carbon dioxide recompression cycle based on small-scale lead-cooled fast reactor, *Int. J. Energy Res.* 46 (2022) 13570–13589, <https://doi.org/10.1002/er.8076>.
- [23] M. Saeed, S. Khatoon, M.H. Kim, Design optimization and performance analysis of a supercritical carbon dioxide recompression Brayton cycle based on the detailed models of the cycle components, *Energ. Convers. Manage.* 196 (2019) 242–260, <https://doi.org/10.1016/j.enconman.2019.05.110>.
- [24] L. Yao, Z. Zou, A one-dimensional design methodology for supercritical carbon dioxide Brayton cycles: Integration of cycle conceptual design and components preliminary design, *Appl. Energy* 276 (2020) 115354, <https://doi.org/10.1016/j.apenergy.2020.115354>.
- [25] I.W. Son, Y.H. Jeong, Y.J. Choi, J.I. Lee, Feasibility study of solar-nuclear hybrid system for distributed power source, *Energ. Convers. Manage.* 230 (2021) 113808, <https://doi.org/10.1016/j.enconman.2020.113808>.
- [26] I.W. Son, Y. Jeong, S. Son, J.H. Park, J.I. Lee, Techno-economic evaluation of solar-nuclear hybrid system for isolated grid, *Appl. Energy* 306 (2022) 118046, <https://doi.org/10.1016/j.apenergy.2021.118046>.
- [27] K. Brun, P. Friedman, R. Dennis, Turbomachinery, in: T.C. Allison, J. Moore, R. Pelton, J. Wilkes, B. Ertas (Eds.), *Fundamentals and applications of supercritical carbon dioxide (SCO₂) based power cycles*, Woodhead publishing, 2017, pp. 47–215. DOI: 10.1016/B978-0-08-100804-1.00007-4.
- [28] O. Olumayegun, M. Wang, G. Kelso, Thermodynamic analysis and preliminary design of closed Brayton cycle using nitrogen as working fluid and coupled to small modular Sodium-cooled fast reactor (SM-SFR), *Appl. Energy* 191 (2017) 436–453, <https://doi.org/10.1016/j.apenergy.2017.01.099>.
- [29] J.M.P. Tournier, M.S. El-Genk, Properties of noble gases and binary mixtures for closed Brayton Cycle applications, *Energ. Convers. Manage.* 49 (2008) 469–492, <https://doi.org/10.1016/j.enconman.2007.06.050>.
- [30] C. Guan, X. Chai, T. Zhang, X. Liu, Preliminary lightweight core design analysis of a micro-transportable gas-cooled thermal reactor, *Int. J. Energy Res.* 46 (2022) 17416–17428, <https://doi.org/10.1002/er.8408>.
- [31] P.K. Romano, N.E. Horelik, B.R. Herman, A.G. Nelson, B. Forget, K. Smith, OpenMC: A state-of-the-art Monte Carlo code for research and development, *Ann. Nucl. Energy* 82 (2015) 90–97, <https://doi.org/10.1016/j.anucene.2014.07.048>.
- [32] M.S. El-Genk, J.M. Tournier, A review of refractory metal alloys and mechanically alloyed-oxide dispersion strengthened steels for space nuclear power systems, *Journal of Nuclear Materials*. 340 (2005) 93–112, <https://doi.org/10.1016/j.jnucmat.2004.10.118>.
- [33] Y.G. Dragunov, V.P. Smetannikov, B.A. Gabaraev, M.S. Belyakov, P.V. Kobzev, On the choice of correlations for calculating the heat transfer coefficient in binary gas mixtures, *J. Eng. Thermophys.* 22 (2013) 30–42, <https://doi.org/10.1134/S1810232813010050>.
- [34] J. Lian, D. Xu, H. Chang, Z. Xu, X. Lu, Q. Wang, T. Ma, Thermal and mechanical performance of a hybrid printed circuit heat exchanger used for supercritical carbon dioxide Brayton cycle, *Energ. Convers. Manage.* 245 (2021) 114573, <https://doi.org/10.1016/j.enconman.2021.114573>.
- [35] A. Moisseytsev, J.J. Sienicki, PDC: Plant Dynamics Code for Design and Transient Analysis of Supercritical Brayton Cycles, United States (2018), <https://doi.org/10.2172/1483844>.
- [36] D. Fleming, T. Holschuh, T. Conboy, G. Rochau, R. Fuller, Scaling considerations for a multi-megawatt class supercritical CO₂ Brayton cycle and path forward for commercialization. Proceedings of the ASME Turbo Expo 2012: Turbine Technical Conference and Exposition. 5 (2012) 953–960. DOI: 10.1115/GT2012-68484.
- [37] S.J. Bae, J. Lee, Y. Ahn, J.I. Lee, Preliminary studies of compact Brayton cycle performance for small modular high temperature gas-cooled reactor system, *Ann. Nucl. Energy* 75 (2015) 11–19, <https://doi.org/10.1016/j.anucene.2014.07.041>.
- [38] R.H. Aungier, Centrifugal Compressors: A Strategy for Aerodynamic Design and Analysis, ASME Press (2000), <https://doi.org/10.1115/1.800938>.
- [39] S. A. Wright, T. M. Conboy, G. E. Rochau, Break-even Power Transients for two Simple Recuperated S-CO₂ Brayton Cycle Test Configurations. Albuquerque, NM, United States, 2011.
- [40] A. Whitfield, The Preliminary Design of Radial Inflow Turbines, *J. Turbomach.* 112 (1990) 50–57, <https://doi.org/10.1115/1.2927420>.
- [41] C. Xu, R.S. Amano, Empirical design considerations for industrial centrifugal compressors, *Int. J. Rotating Mach.* 2012 (2012) 184061, <https://doi.org/10.1155/2012/184061>.
- [42] A. Meroni, B. Zühlstorff, B. Elmegård, F. Haglind, Design of centrifugal compressors for heat pump systems, *Appl. Energy* 232 (2018) 139–156, <https://doi.org/10.1016/j.apenergy.2018.09.210>.
- [43] F.J. Wiesner, A review of slip factors for centrifugal impellers. *Journal of Engineering for Power*. 89 (1967) 558–572, <https://doi.org/10.1115/1.3616734>.
- [44] B. Monge Briones, *Design of supercritical carbon dioxide centrifugal compressors*. Tesis Doctoral Inédita, Universidad de Sevilla, Sevilla, 2014.
- [45] H. E. Rohlik, Analytical determination of radial inflow turbine design geometry for maximum efficiency. NASA TND-4384, United States, 1968.
- [46] J. F. Suhrmann, D. Peitsch, M. Gugau, T. Heuer, U. Tomm, Validation and development of loss models for small size radial turbines. Proceedings of the ASME Turbo Expo 2010: Power for Land, Sea, and Air. 7 (2010) 1937–1949. DOI: 10.1115/GT2010-22666.
- [47] C.A. Ventura, P.A. Jacobs, A.S. Rowlands, P. Petrie-Repar, E. Sauret, Preliminary design and performance estimation of radial inflow turbines: an automated approach, *J. Fluids Eng.* 134 (2012) 031102, <https://doi.org/10.1115/1.4006174>.